Atmos. Chem. Phys. Discuss., 14, 23499–23554, 2014
www.atmos-chem-phys-discuss.net/14/23499/2014/
doi:10.5194/acpd-14-23499-2014

Atmospheric Chemistry and Physics Discussions

SO_2 photolysis as a source for sulfur mass-independent isotope signatures in stratospheric aerosols

A. R. Whitehill[1], **B. Jiang**[2], **H. Guo**[2], **and S. Ono**[1]

[1]Department of Earth, Atmospheric, and Planetary Sciences, Massachusetts Institute of Technology, 77 Massachusetts Ave., Cambridge, MA 02139, USA
[2]Department of Chemistry and Chemical Biology, University of New Mexico, Albuquerque, NM 87131, USA

Received: 14 August 2014 – Accepted: 29 August 2014 – Published: 12 September 2014

Correspondence to: A. R. Whitehill (arwhite@mit.edu)

Published by Copernicus Publications on behalf of the European Geosciences Union.

Abstract

Signatures of sulfur isotope mass-independent fractionation (S-MIF) have been observed in stratospheric sulfate aerosols deposited in polar ice. The S-MIF signatures are associated with stratospheric photochemistry following stratospheric volcanic eruptions, but the exact mechanism responsible for the production and preservation of these signatures is debated. In order to identify the origin and the mechanism of preservation for these signatures, a series of laboratory photochemical experiments were carried out to investigate the effect of temperature and added O_2 on S-MIF produced by the two absorption band systems of SO_2 photolysis in the 190 to 220 nm region and photoexcitation in the 250 to 350 nm region. The SO_2 photolysis ($SO_2 + h\nu \rightarrow SO + O$) experiments showed S-MIF signals with large $^{34}S/^{32}S$ fractionation, which increases with decreasing temperature. The overall S-MIF pattern observed for photolysis experiments, including high $^{34}S/^{32}S$ fractionations, positive mass-independent anomalies in ^{33}S, and negative anomalies in ^{36}S, is consistent with a major contribution from optical isotopologue screening effects and measurements for stratospheric sulfate aerosols. SO_2 photoexicitation produced products with positive MIF anomalies in both ^{33}S and ^{36}S that is different from stratospheric aerosols. SO_2 photolysis in the presence of O_2 produced SO_3 with S-MIF signals, suggesting the transfer of the MIF signals of SO to SO_3 by the $SO + O_2 + M \rightarrow SO_3 + M$ reaction. This is supported with energy calculations of stationary points on the SO_3 potential energy surfaces, which indicate that this reaction occurs slowly on a single adiabatic surface, but that it can occur more rapidly through intersystem crossing. The results from our experiments constrain the termolecular reaction rate to between 1.0×10^{-37} cm^6 molecule^{-2} s^{-1} and 1.0×10^{-36} cm^6 molecule^{-2} s^{-1}. This rate can explain the preservation of mass independent isotope signatures in stratospheric sulfate aerosols and provides a minor, but important, oxidation pathway for stratospheric SO_2 above about 25 km altitude. The production and preservation of S-MIF signals in the stratosphere requires a high SO_2 column density and an SO_2 plume reaching an altitude of 25 km and higher.

ACPD
14, 23499–23554, 2014

1 Introduction

Explosive volcanic eruptions that inject sulfur dioxide (SO_2) into the stratosphere can cause perturbations to the stratospheric sulfur cycle for years following eruptions. The increase in stratospheric sulfate aerosols associated with injections of SO_2 result in stratospheric warming and tropospheric cooling, and can also trigger changes in atmospheric circulation and increases in ozone depletion (Robock, 2000). Perturbations to the stratospheric sulfur cycle following large volcanic eruptions are recorded as changes in sulfur isotope ratios, as measured in stratospheric sulfate aerosol samples (Castleman et al., 1974), as well as in ice core records (Savarino et al., 2003; Baroni et al., 2007).

The reaction with OH is the dominant oxidation pathway for SO_2 in the stratosphere:

$$SO_2 + OH + M \rightarrow HOSO_2 + M \quad \text{(R1)}$$

This reaction is followed by:

$$HOSO_2 + O_2 \rightarrow SO_3 + HO_2 \quad \text{(R2)}$$

In the presence of H_2O, SO_3 readily forms sulfuric acid (H_2SO_4) via:

$$SO_3 + H_2O \rightarrow H_2SO_4 \quad \text{(R3)}$$

Ab-initio transition state theory calculations of the isotope effect for OH oxidation (R1) predict that $^{34}SO_2$ is oxidized 0.9 % slower than $^{32}SO_2$ (Tanaka et al., 1994), although calculations with RRKM theory predicts an inverse isotope effect, in which $^{34}SO_2$ reacts 12 % to 15 % faster than $^{32}SO_2$ (Leung et al., 2001). Experimental studies of OH oxidation (R1) showed an inverse isotope effect, but with a smaller magnitude, with $^{34}SO_2$ reacting about 1 % faster than $^{32}SO_2$ (Harris et al., 2012). The experimentally measured isotope effect is insufficient to explain the roughly 2 % enrichment in $H_2^{34}SO_4$

ACPD
14, 23499–23554, 2014

relative to $H_2^{32}SO_4$ following the major Mt. Agung (1963) eruption (Castleman et al., 1974). An additional oxidation reaction is necessary to explain the sulfur isotope effects in stratospheric sulfate aerosols following large volcanic eruptions.

An additional unexplained observation is the isotope anomalies in $^{33}S/^{32}S$ and $^{36}S/^{32}S$ ratios relative to $^{34}S/^{32}S$ ratios. These signatures of mass-independent fractionation (MIF) have been observed in ice cores associated with large volcanic eruptions (Savarino et al., 2003; Baroni et al., 2007, 2008; Lanciki, 2010; Lanciki et al., 2012). Ice core sulfate peaks are commonly used to reconstruct the impact of past volcanic activity, which is critical to forcing climate models (Robock, 2000). For several years following large injections of SO_2 into the stratosphere, stratosphere-derived sulfate can dominate sulfate deposition in ice cores and, if corrected for background levels, can preserve the sulfur isotopic composition of stratospheric sulfate aerosols. Experimental studies demonstrate that OH oxidation of SO_2 (R1) does not produce mass-independent sulfur isotope anomalies (Harris et al., 2012, 2013), so an additional oxidation mechanism is required to produce the mass-independent sulfur isotope signatures. Three reactions have been proposed to explain these isotope anomalies: excited-state photochemistry of SO_2 in the 250 to 350 nm absorption region (Savarino et al., 2003; Hattori et al., 2013), SO_2 photolysis in the 190 to 220 nm absorption region (Ono et al., 2013), and SO_3 photolysis (Pavlov et al., 2005).

We present results of laboratory photochemical experiments that support SO_2 photolysis as the source for the MIF signatures observed in stratospheric sulfate aerosols following some large (stratospheric) volcanic eruptions. In particular, SO_2 photolysis produces large MIF anomalies, as well as large mass-dependent isotope fractionations (Masterson et al., 2011; Whitehill and Ono, 2012; Ono et al., 2013) that are consistent with the isotopic signatures observed in stratospheric sulfate aerosols in ice cores (Ono et al., 2013). Even a minor contribution of SO_2 photolysis to the production of sulfate aerosols can have a major influence on the isotope ratios of sulfur.

Photolysis of SO_2 occurs above 25 km in the wavelength region of 190 to 220 nm, which lies in the spectral window between the Schumann–Runge absorption edge of

ACPD
14, 23499–23554, 2014

oxygen (O_2) and the Hartley bands of ozone (O_3). SO_2 photolysis produces sulfur monoxide (SO) and $O(^3P)$ via the following reaction:

$$SO_2 + h\nu \rightarrow SO + O(^3P) \quad \text{(R4)}$$

It is generally accepted that this reaction is followed by rapid oxidation of SO to SO_2 via (Black et al., 1982; Savarino et al., 2003; Pavlov et al., 2005):

$$SO + O_2 \rightarrow SO_2 + O(^3P) \quad \text{(R5)}$$

Reactions (R4) and (R5) combine to form a null cycle for sulfur, but catalyze the formation of odd oxygen (Bekki, 1995). If SO is completely oxidized to SO_2, no isotopic signature from SO_2 photolysis can be preserved (Pavlov et al., 2005).

We propose an additional channel where SO is oxidized directly to SO_3 via the termolecular reaction:

$$SO + O_2 + M \rightarrow SO_3 + M \quad \text{(R6)}$$

A previous study by Black et al. (1982) showed that the maximum termolecular rate constant for Reaction (R6) is 10^{-36} cm^6 molecule^{-2} s^{-1}. This rate is considered too slow to play an important role for stratospheric chemistry (Black et al., 1982). However, given the large isotope effects produced during SO_2 photolysis, even a minor contribution from R6 will produce a significant signal on the sulfur isotopic composition of stratospheric sulfate aerosols.

We present results from laboratory photochemical experiments that investigate the effect of temperature and molecular oxygen on the isotope effects produced during SO_2 photolysis (190 to 220 nm) and SO_2 photoexcitation (250 to 350 nm). Using the results of the experiments in the presence of molecular oxygen, we calculate a lower bound estimate on the rate of R6. In addition, our proposal is further supported by ab-initio calculations of stationary points along the potential energy surfaces (PESs) for the SO oxidation Reactions (R5) and (R6). Finally, we present a simple steady state

ACPD
14, 23499–23554, 2014

photochemical model to show that the rate constraints on Reaction (R6) are sufficient for it to make a significant contribution to the isotopic signature of stratospheric sulfate aerosols during volcanically perturbed periods.

2 Methods

2.1 Photochemical reaction set-up

Conditions for all photochemical experiments are listed in Table 1. All experiments were performed in a cylindrical glass photochemical reaction cell with a pathlength of 15.3 cm and an inner diameter of 5.2 cm (Ono et al., 2013). Temperature-controlled experiments were performed in a jacketed cell of the same dimensions. The front window of the cell was made of UV-grade SiO_2 (Corning 7980) with greater than 90 % transmittance above 190 nm. The window was sealed to the cell with an o-ring and held in place securely with a plastic clamp. Temperature-controlled experiments also utilized a second pre-cell (5.3 cm pathlength) attached to the front window of the reaction cell and held under vacuum. The purpose of the pre-cell was to thermally insulate the front window and prevent condensation from occurring on the front window during low temperature experiments.

A series of mass-flow controllers controlled the flow rate of gases into the cell. Gas entered the cell through an inlet at the rear of the cell (for temperature cell experiments) or the front of the cell (for other experiments) and exited the cell through an outlet at the opposite end of the cell. An 8 cm to 10 cm length of glass tubing packed with glass wool was placed immediately after the cell exit to trap aerosols formed within the cell. Following the aerosol trap, the gas was flowed through a proportionating valve to a vacuum pump. A capacitance manometer placed before the entrance to the cell monitored the pressure within the cell. The proportionating valve was used to control the pressure within the cell to within 30 Pa of a setpoint pressure, which was usually 101.3 kPa.

ACPD
14, 23499–23554, 2014

Prior to each temperature-controlled experiment, the reaction cell was flushed with nitrogen (N_2) for several hours and the chiller was allowed to reach its setpoint temperature and equilibrate for at least an hour. The temperature of the reaction cell was calibrated relative to the chiller setpoint temperature on two occasions using a series of K-type thermocouples suspended within the cell. During calibrations, N_2 was flowed through the cell at a rate of 3.33 $cm^3 s^{-1}$ (200 sccm, standard cubic centimeter per minute). Thermocouples placed at the front and rear of the cell gave consistent measurements to within 5 K, with a higher gradient at lower temperatures. No significant differences were observed between the two calibrations. Results for the temperature calibration are shown in Fig. 1.

2.2 Temperature effect on SO_2 photolysis (190 to 220 nm) and photoexcitation (250 to 350 nm)

The temperature effect on SO_2 photolysis (190 to 220 nm) was measured using the temperature-controlled reaction cell described in Sect. 2.1. Experiments were performed in a nitrogen-flushed glove box to prevent the spectral interference from the Schumann–Runge band of oxygen (O_2). A 200 W deuterium (D_2) arc lamp (D 200 F, Heraeus Noblelight) was used as the light source without optical filters. The output from the lamp was collimated using a fused silica plano-convex lens. 1000 ppm SO_2 (in N_2) was flowed through the cell at a rate of 3.33 $cm^3 s^{-1}$ (200 sccm) for all experiments, and pressure within the cell was held constant at 101.3 kPa, giving an SO_2 partial pressure of 0.10 kPa within the cell.

Following photolysis experiments, the cell was removed from the glove box and rinsed well with dichloromethane (DCM) to dissolve any elemental sulfur that was formed. The glass wool in the aerosol trap was also collected and rinsed with DCM. Elemental sulfur was recrystallized from DCM and converted to silver sulfide using the reduced chromium chloride method (Whitehill and Ono, 2012; Canfield et al., 1986). Multiple sulfur isotope ratios were measured as described in Sect. 2.4.

ACPD
14, 23499–23554, 2014

Photoexcitation experiments were performed in a room air atmosphere using a 150 W UV-enhanced xenon (Xe) arc lamp (Newport Model 6254) housed in a lamp housing (Newport Model 67005), which focused and collimated the light to a 3.3 cm diameter beam. The light was passed through a liquid filter (Newport Model 51945) filled with deionized (18.2 MΩ) water and a 250 nm longpass filter (Asahi Spectra, ZUL0250).

Following Whitehill et al. (2013), acetylene (C_2H_2) was used to trap triplet excited-state SO_2 ($^3SO_2$). During experiments, 5 % SO_2 (in N_2), pure C_2H_2 (Atomic Absorption Grade), and pure N_2 (Ultra High Purity grade) were flowed through the cell continuously at a rate of 0.67 $cm^3\,s^{-1}$ (40 sccm), 0.03 $cm^3\,s^{-1}$ (2 sccm), and 2.63 $cm^3\,s^{-1}$ (158 sccm), respectively. Pressure in the cell was held constant at 101.3 kPa, giving a total flow rate of 3.33 $cm^3\,s^{-1}$, an SO_2 partial pressure of 1.01 kPa, and a C_2H_2 partial pressure of 1.01 kPa within the cell during the experiments.

Following the experiments, the interior walls of the cell and the window were rinsed with ethanol and water to dissolve any organosulfur products formed. The glass wool in the aerosol trap was also collected. The organosulfur aerosol products were converted to silver sulfide using the Raney nickel hydrodesulfurization method of Oduro et al. (2011). Multiple sulfur isotope ratios were measured as described in Sect. 2.4.

2.3 SO_2 photochemistry in the presence of O_2

The photochemistry of $SO_2 + O_2$ with ultraviolet radiation was studied using a reaction cell at room temperature. The 150 W Xe arc lamp (described in Sect. 2.2) was used as the light source without the liquid filter. Several experiments were performed with a 200 ± 35 nm bandpass filter (Model 200-B, Acton Research, Acton, MA), a 250 nm longpass filter (Asahi Spectra, ZUL0250), or a 280 nm (285 nm cut-on) longpass filter (Newport Model FSR-WG280) to isolate particular absorption bands of SO_2, but most experiments were performed with the Xe lamp and no filters.

Following experiments, the cell was rinsed well first with dichloromethane (DCM) then with water. Although sulfate was the dominant product, the cell was rinsed well

ACPD
14, 23499–23554, 2014

with DCM first to ensure the removal of elemental sulfur. For two experiments performed with no oxygen, elemental sulfur was recovered. After rinsing the cell with water, 5.0 cm^3 of a 1.0 $mol\,dm^{-3}$ solution of barium chloride ($BaCl_2$) was added to the water used to rinse the cell to precipitate sulfate as barium sulfate. Barium sulfate was rinsed several times with deionized water and dried. The glass wool inside the aerosol trap was combined with the barium sulfate and all sulfate was converted to silver sulfide using the method of Forrest and Newman (1977). Multiple sulfur isotope ratios were measured as described in Sect. 2.4.

2.4 Isotope analysis of photochemical products

Photochemical products were converted to silver sulfide (Ag_2S). Ag_2S was rinsed well three to four times with deionized water and then dried completely at 353 K. Dried Ag_2S was weighed for total yield and about 8 µmol of Ag_2S was weighed into an aluminum foil capsule for isotope analysis. Capsules were loaded into nickel reaction chambers and reacted under approximately 7.3 kPa of fluorine gas (F_2) for at least 8 h at 573 K. The resultant SF_6 was purified cryogenically and by gas chromatography. Isotope ratios of pure SF_6 were measured as SF_5^+ ions using a Thermo Scientific MAT 253 Isotope Ratio Mass Spectrometer. For samples where less than 1.6 µmol of Ag_2S was recovered, a microvolume (0.4 cm^3 volume) coldfinger was used to concentrate the samples for analysis.

Replicate analyses ($N = 28$) of the reference material IAEA-S-1 gave 2σ standard deviations of 0.26 ‰ for $\delta^{34}S$, 0.014 ‰ for $\Delta^{33}S$, and 0.19 ‰ for $\Delta^{36}S$ for standard isotope ratio mass spectrometry analysis. Microvolume analyses for smaller samples gave 2σ standard deviations for replicate analyses of IAEA-S-1 ($N = 14$) of 0.9 ‰ for $\delta^{34}S$, 0.08 ‰ for $\Delta^{33}S$, and 0.8 ‰ for $\Delta^{36}S$. Replicate experiments performed under identical conditions had differences larger than the analytical uncertainty, suggesting experimental variability was the dominant source of uncertainty in our measurements.

ACPD
14, 23499–23554, 2014

2.5 Potential energy surfaces of $SO + O_2 \rightarrow SO_3 \rightarrow SO_2 + O$ reactions

To test the feasibility of Reaction (R6), ab-initio energy calculations at multiple levels of theory were performed to search important stationary points on the SO_3 potential energy surfaces (PESs). The lowest $SO(^3\Sigma^-) + O_2(^3\Sigma_g^-)$ asymptote of the SO_3 PESs involves three degenerate states, namely the singlet, triplet, and quintet states. The singlet state corresponds to the ground state of the SO_3 molecule ($^1A_1'$), but does not dissociate to the ground state products $SO_2(^1A_1) + O(^3P)$ but to $SO_2(^1A_1) + O(^1D)$. The triplet surface corresponds to the ground state products but is adiabatically associated with a higher energy excited-state (triplet) SO_3. The quintet state is much higher in energy than the other two states except at the $SO(^3\Sigma^-) + O_2(^3\Sigma_g^-)$ asymptote and will thus not be considered in this study.

The B3LYP density functional (Becke, 1988; Lee et al., 1988) was initially used to optimize each minimum and/or transition state on the singlet and triplet potential energy surfaces. Single point calculations at these stationary points were then carried out using an explicitly correlated version of the unrestricted coupled cluster method with single, double and perturbative triple excitations method (UCCSD(T)-F12a; Knizia et al., 2009).

In addition, complete active space self consistent field (CASSCF) calculations were performed (Knowles and Werner, 1985, 1988). Multi-reference Rayleigh Schrodinger perturbation theory of second order (RSPT2 or CASPT2) calculations (Celani and Werner, 2000) were performed based on the CASSCF wavefunctions in order to account for part of the dynamical correlation. Calculations including the full valence orbitals would involve 24 electrons in 16 orbitals and were not feasible. Instead, the 2 s orbital for O and the 3 s orbital for S were closed, resulting in an active space of 16 electrons in 12 orbitals (16,12). Dunning's augmented correlation-consistent polarized valence triplet-zeta (aug-cc-pVTZ) basis set was used in all cases (Dunning, 1989). B3LYP calculations were performed with Gaussian09 (Frisch et al., 2009) and the other calculations were performed using MOLPRO (Werner et al., 2012).

ACPD
14, 23499–23554, 2014

2.6 Definitions

Isotopic results will be presented with conventional δ notation, as relative deviations of isotope ratios with respect to reference sulfur.

$$\delta^x S = \frac{{}^x R_{\text{product}}}{{}^x R_{\text{reference}}} - 1 \quad (1)$$

where $x = 33$, 34, or 36 and ${}^x R$ is the ratio of ${}^x S$ to ${}^{32}S$ in the substance. For experimental results all isotope ratios will be normalized to the isotope ratios of the initial SO_2. For natural samples (i.e. stratospheric sulfate aerosol samples), the reference is Vienna Canyon Diablo Troilite (V-CDT).

Mass-independent isotope fractionations in ${}^{33}S/{}^{32}S$ and ${}^{36}S/{}^{32}S$ ratios (relative to ${}^{34}S/{}^{32}S$ ratios) will be presented as $\Delta^{33}S$ and $\Delta^{36}S$ values, respectively. These are defined as:

$$\Delta^{33}S = \frac{(\delta^{33}S + 1)}{(\delta^{34}S + 1)^{0.515}} - 1 \quad (2)$$

and

$$\Delta^{36}S = \frac{(\delta^{36}S + 1)}{(\delta^{34}S + 1)^{1.90}} - 1 \quad (3)$$

Almost all physical, chemical, and biological processes fractionate isotopes mass-dependently (i.e. $\Delta^{33}S = 0$ and $\Delta^{36}S = 0$). SO_2 photochemistry, as well as the photochemistry of other sulfur gases such as CS_2, are some of the few exceptions that produce mass-independent fractionation. Therefore, non-zero $\Delta^{33}S$ and $\Delta^{36}S$ values can be unique tracers of photochemical processes.

ACPD
14, 23499–23554, 2014

3 Results

All experiments performed are summarized in Table 1. Results from temperature experiments on SO_2 photolysis and SO_2 photoexcitation are given in Tables 2 and 3, whereas results from $SO_2 + O_2$ experiments are presented in Tables 4 and 5. Tables 6–8 give the results from energy calculations on the potential energy surfaces of SO_3.

3.1 Temperature experiments

Results from the temperature experiments (Sect. 2.2) are shown in Fig. 2. The SO_2 photolysis (190 to 220 nm) experiments (Table 2) revealed that the magnitude of the isotope effects increase with decreasing temperatures, from 129 ‰ to 191 ‰, 5.5 ‰ to 9.1 ‰ and −24.1 ‰ to −35.8 ‰, for $\delta^{34}S$, $\Delta^{33}S$, and $\Delta^{36}S$, respectively. The relationship between isotopes (i.e. $\Delta^{33}S$ vs. $\delta^{34}S$ and $\Delta^{36}S$ vs. $\Delta^{33}S$) did not change significantly as temperature was decreased (0.04 to 0.05 for $\Delta^{33}S/\delta^{34}S$ and −3.9 to −4.6 for $\Delta^{36}S/\Delta^{33}S$). SO_2 photoexcitation (250 to 350 nm) show decreasing magnitude $\Delta^{33}S$ and $\Delta^{36}S$ values at lower temperatures (22.8 ‰ to 19.0 ‰ and 52.5 ‰ to 46.0 ‰ for $\Delta^{33}S$ and $\Delta^{36}S$, respectively; Table 3). Even at lower temperatures, the product from SO_2 photoexcitation experiments show positive $\Delta^{33}S$ and $\Delta^{36}S$ values, as shown previously in room-temperature experiments (Whitehill and Ono, 2012; Whitehill et al., 2013).

3.2 Oxygen experiments

SO_2 photolysis and photoexcitation in the presence of molecular oxygen (O_2) produced mass-independent sulfur isotope signatures in sulfate products (Tables 4 and 5). Isotope ratios of this product sulfate are shown in Fig. 3 and compared with stratospheric sulfate aerosol data from ice cores (Savarino et al., 2003; Baroni et al., 2007, 2008; Lanciki, 2010; Lanciki et al., 2012). Strong agreement between the Xe lamp data, 200 nm bandpass (200 BP) data, and previous SO_2 photolysis data (Ono et al.,

ACPD
14, 23499–23554, 2014

2013) suggest an SO_2 photolysis source for the isotope effects during broadband SO_2 irradiation with the Xe lamp light source.

Experiments focusing on the photoexcitation band of SO_2 using the 250 nm longpass filter (250 LP) and 280 nm longpass filter (280 LP) display a different isotope signature, characterized by positive $\Delta^{33}S$ and $\Delta^{36}S$ values, whereas sulfate from SO_2 photolysis has positive $\Delta^{33}S$ and negative $\Delta^{36}S$ values. This is consistent with previous findings (Whitehill and Ono, 2012; Whitehill et al., 2013), and demonstrates the MIF in this band region is not produced by chemistry related to acetylene nor oxygen.

3.3 Potential energy surfaces of SO_3

Asymptotic energies of $SO + O_2$ on each potential energy surface were compared with the energies obtained by separate calculations of each species with a certain spin (Table 6). CASSCF results correctly produced degenerate energies for the $SO+O_2$ asymptote on the singlet and triplet states, which exactly match the sum of the energies on the $SO(^3\Sigma^-)$ and $O_2(^3\Sigma_g^-)$ calculated separately. CASPT2 results also show the correct degenerate behavior but the energies shift slightly from those calculated separately, which presumably arises from the perturbation. On the other hand, UCCSD(T)-F12a and B3LYP results both attribute $SO+O_2$ on the singlet state to $SO(^1\Delta) + O_2(^1\Delta_g)$, and B3LYP even gives a qualitatively incorrect energy for $SO + O_2$ on the triplet state, while UCCSD(T)-F12a attributes this one to $SO(^1\Delta) + O_2(^3\Sigma_g^-)$. An important conclusion from these data is that one has to use a multi-reference method if an accurate global adiabatic potential energy surface is desired for this system. Otherwise, the asymptotic behavior can be completely wrong. None of the previous studies has noticed this, and as a result a single-reference method was always selected (Jou et al., 1996; Martin, 1999; Goodarzi et al., 2010; Ahmed, 2013). Fortunately, single reference methods can accurately describe the PES away from the $SO + O_2$ region; they are capable of describing several SO_3 isomers and the $SO_2 + O$ product channel reasonably well.

ACPD
14, 23499–23554, 2014

Energies for the stationary points computed using multi-reference approaches are reported relative to that of the $SO(^3\Sigma^-) + O_2(^3\Sigma_g^-)$ asymptote. However, the active space used in our CASSCF calculations is not sufficient to provide quantitatively accurate results, but a larger active space is still computationally infeasible. For single-reference calculations, we chose to use the UCCSD(T) energies at optimized B3LYP geometries for the stationary points. To avoid the aforementioned problems in the $SO(^3\Sigma^-) + O_2(^3\Sigma_g^-)$ asymptote, we have used the UCCSD(T) energy sum of the two reactants with the correct spins calculated separately, which has been shown to be accurate. The sum of these two energies thus provides the reference for other stationary points on both singlet and triplet PESs. All energies of stationary points are listed in Tables 7 and 8, and the reaction pathways on both PESs are shown graphically in Fig. 4, using the energies of the UCCSD(T)//B3LYP calculations. It is seen from Tables 7 and 8 that the experimental derived energy differences (from Chase, 1986) between reactants and products for the $SO(^3\Sigma^-) + O_2(^3\Sigma_g^-) \rightarrow SO_3(^1A_1')$ reaction ($-411.29\,kJ\,mole^{-1}$), the $SO(^3\Sigma^-) + O_2(^3\Sigma_g^-) \rightarrow SO_2(^1A_1) + O(^3P)$ reaction ($-54.56\,kJ\,mole^{-1}$) and the $SO(^3\Sigma^-) + O_2(^3\Sigma_g^-) \rightarrow SO_2(^1A_1) + O(^1D)$ reaction ($135.27\,kJ\,mole^{-1}$) are reproduced well by the UCCSD(T)-F12a//B3LYP calculations, while the other methods contain significant errors.

4 Discussion

4.1 Origin of mass-independent fractionation during SO_2 photochemistry

Isotopologue-specific absorption cross sections are expected to correctly predict the isotope effects from SO_2 photolysis (in the 190 to 220 nm region) but fail to reproduce the isotope effects from SO_2 photoexcitation (in the 250 to 350 nm region). This is due to the differences in the photophysics and photochemistry between the two absorption regions, which result in different mechanisms for MIF formation (Whitehill and Ono, 2012; Ono et al., 2013; Whitehill et al., 2013).

ACPD
14, 23499–23554, 2014

In the 165 to 235 nm wavelength region, SO_2 photolysis occurs through predissociation from the bound $\tilde{C}(^1B_2)$ state. Near the dissociation threshold of 218.7 nm (Becker et al., 1995), the quantum yield of photolysis is less than unity, although it increases to greater than 0.99 at wavelengths shorter than 215 nm (Katagiri et al., 1997). In the region where the quantum yield is close to unity (i.e. less than 215 nm), the isotope effects due to SO_2 photolysis should be determined entirely by the differences in the absorption cross-sections between the different isotopologues of SO_2 (e.g., by isotopologue specific Franck–Condon coupling; Danielache et al., 2008) and optical screening effects under high SO_2 column densities (Lyons, 2007, 2008; Ono et al., 2013). In the narrow spectral region from 215 to 218.7 nm, where the quantum yield of photodissociation varies, it is possible that quantum yield differences between isotopologues could potentially produce additional isotope effects beyond those predicted from absorption cross-sections. However, in this region, photodissociation occurs primarily via vibronic mixing of the $\tilde{C}(^1B_2)$ state levels with the dissociative continuum of the electronic ground, $\tilde{X}(^1A_1)$ state (Katagiri et al., 1997). Due to the high density of vibronic levels for the $\tilde{X}(^1A_1)$ state, it is unlikely that there will be significant isotope effects in the coupling strength between the $\tilde{C}(^1B_2)$ and $\tilde{X}(^1A_1)$ states. Dissociation occurring through mixing with repulsive singlet and triplet states is expected to be small, as is the nonadiabatic coupling of the $\tilde{C}(^1B_2)$ and $\tilde{D}(^1A_1)$ states (Tokue and Nanbu, 2010).

For laboratory experiments, the observed isotope effects for SO_2 photolysis is a function not only of differences in the absorption cross-sections (Danielache et al., 2008) but also a function of the SO_2 column density. This is because the SO_2 absorption cross-section has significant fine structure, which causes optical screening effects to occur (Lyons, 2007). This optical screening effect produces larger isotope effects at higher SO_2 column densities (Ono et al., 2013). In addition to the above effects, there appears to be a total (or bath gas) pressure effect on $\Delta^{33}S$ values. This manifests as reduced $\Delta^{33}S$ values at higher total (i.e. bath gas) pressures, which is observed with He, SO_2, and N_2 bath gases (Masterson et al., 2011; Whitehill and Ono, 2012; Ono et al., 2013). The mechanism responsible for these pressure effects is still uncertain,

ACPD
14, 23499–23554, 2014

but it could suggest that $^{33}SO_2$ has a longer excited-state lifetime prior to dissociation than the other isotopologues.

SO_2 photoexcitation in the 250 to 350 nm absorption region produces isotope effects by a completely different mechanism. SO_2 photoexcitation in the 250 to 350 nm region occurs by initial excitation into a coupled $\tilde{A}(^1A_2)/\tilde{B}(^1B_1)$ singlet excited state that undergoes intersystem crossing to the photochemically active triplet $\tilde{a}(^3B_1)$ state (Xie et al., 2013; Lévêque et al., 2014). Unlike SO_2 photolysis, where the quantum yield of reaction (i.e. photolysis) is near unity, the quantum yield for intersystem crossing between the singlet and triplet states is highly variable and state-dependent. Due to the relatively low density of states in the crossing region ($\tilde{A}^1A_2 \rightarrow \tilde{a}^3B_1$), the branching between quenching to the ground state and intersystem crossing to the triplet state will be a strong function of isotope substitution. Whitehill et al. (2013) argue that this isotope selective intersystem crossing as the origin of most of the isotope effects in photochemical products following SO_2 photoexcitation in the 250 to 350 nm absorption region.

Photoexcitation of SO_2 in the presence of O_2 produces sulfate with both positive $\Delta^{33}S$ and positive $\Delta^{36}S$ signals, similar to the organic sulfur observed in Whitehill et al. (2013) and the elemental sulfur in Whitehill and Ono (2012). This suggests that the anomalous isotope signatures observed from photoexcitation in previous studies are a result of the photophysics of excited-state SO_2 rather than the photochemistry of subsequent reactions (i.e., the chemistry with acetylene). Our experimental results show significant discrepancy with isotope effects predicted by isotopologue-specific absorption cross-sections (Danielache et al., 2012; Hattori et al., 2013) for the 250 to 320 nm region (Whitehill et al., 2013). This is expected if isotope selective intersystem crossing is overprinting the isotope signals produced by cross section differences.

ACPD
14, 23499–23554, 2014

4.2 Temperature effects on SO_2 photolysis

Lyons (2007, 2008) presented isotopologue-specific absorption cross-sections for SO_2 in the 190 to 220 nm absorption region by shifting the measured $^{32}SO_2$ absorption cross-sections of Freeman et al. (1984) by an amount based on the calculated isotope shifts of Ran et al. (2007). It has been unclear whether these absorption cross-sections can correctly predict the isotope effects due to SO_2 photolysis (Danielache et al., 2008), as they include only isotope shifts and not other potential differences among isotopologues. Previous comparisons with experimental data showed significant discrepancies (i.e. a factor of ~ 2 in $\delta^{34}S$ values) between experimental data and that predicted by the Lyons (2007, 2008) cross-sections (Whitehill and Ono, 2012; Ono et al., 2013). Such discrepancies were attributed to the difference in temperature between the Lyons (2007, 2008) cross-sections, which are based on cross-sections measured at 213 K (Freeman et al., 1984) and the temperature of the experiments (298 K). Given the new temperature data in the present study, it is possible to compare calculations based on the Lyons (2007, 2008) cross-sections with temperature-dependent experimental isotope data. Calculations were performed as described in previous papers (Whitehill and Ono, 2012; Ono et al., 2013) and are compared to experimental data in Fig. 5.

Excellent agreement with the Lyons (2007, 2008) cross-sections can be seen when the observed temperature dependence on $\delta^{34}S$ are extrapolated back to 213 K. A similar strong agreement is also seen in the $\Delta^{36}S$ values. This new data fills in the major gap between predictions based on the Lyons (2007, 2008) cross-sections and the room-temperature experimental data, and provides further support to an optical origin of mass-independent fractionation during SO_2 photolysis (Ono et al., 2013).

Despite the strong agreement for $\delta^{34}S$ and $\Delta^{36}S$ values, the Lyons (2007, 2008) cross-sections over-predict the magnitude of the mass-independent isotope anomaly in ^{33}S (i.e. $\Delta^{33}S$ values) when compared with experimental data. There are several possible explanations for this. One reason is that there are significant differences between the actual cross-sections and those predicted by shifting the $^{32}SO_2$ cross-sections

ACPD
14, 23499–23554, 2014

for $^{33}SO_2$. Measurements by Danielache et al. (2008) at room temperature suggest that there are some differences between the isotopologue-specific absorption cross-sections aside from just the spectral shifts accounted for by Lyons (2007, 2008). A second possibility is that the high total pressure (101.3 kPa, including the N_2 bath gas) of the experiments caused a decrease in the $\Delta^{33}S$ value relative to values observed at lower total pressures. It has been previously observed (Masterson et al., 2011; Whitehill and Ono, 2012; Ono et al., 2013) that $\Delta^{33}S$ values decrease in the presence of high bath gas pressures. This pressure quenching effect is most noticeable for $\Delta^{33}S$ and does not affect $\delta^{34}S$ or $\Delta^{36}S$ values as strongly.

We conclude that the Lyons (2007, 2008) cross sections can accurately predict the isotope effects during SO_2 photolysis under low temperature (ca. 213 K) conditions, such as those in the stratosphere. Conversely, cross sections measured at room temperature (e.g., Danielache et al., 2008) will underestimate $\delta^{34}S$ fractionations when applied to stratospheric conditions.

4.3 Constraining the rate of the SO + O_2 + M reaction using product formation

Our results demonstrate that photolysis of SO_2 in the presence of molecular oxygen (O_2) produces large amounts of sulfate with considerable mass-independent sulfur isotope anomalies. In our experimental system, there are three dominant pathways for SO_3 formation: OH oxidation of SO_2 (Reactions R1 and R2, if water is present), O_2 oxidation of SO from SO_2 photolysis (Reactions R4 and R6), and O oxidation of SO_2 via

$$SO_2 + O + M \rightarrow SO_3 + M \quad \text{(R7)}$$

OH and O oxidation of SO_2 (Reactions R1 and R7) are mass dependent (Harris et al., 2012; Whitehill and Ono, 2012; Ono et al., 2013). However, oxidation of SO via Reaction (R6) will trap the isotopic composition of SO as SO_3 and carry the mass-independent sulfur isotope signature from SO_2 photolysis (Reaction R4).

ACPD
14, 23499–23554, 2014

We performed a series of experiments at a total pressure of 101.3 kPa, a flow rate of 6.67 $cm^3\ s^{-1}$ (400 sccm) and an SO_2 partial pressure of 0.127 kPa (Table 4; Fig. 6). The partial pressure of molecular oxygen was varied from 0 kPa to 19.8 kPa (0 % to 19.5 % O_2). In all experiments, SO_2 was photolyzed via R4. In the experiments with no oxygen, both elemental sulfur (S^o) and SO_3 aerosols were formed, with the elemental sulfur (S and related species) formed from SO via:

$$SO + SO \rightarrow SO_2 + S \quad \text{(R8)}$$

SO photolysis is expected to be a minor source of S compared to Reaction (R8). In the absence of oxygen, SO_3 is formed primarily via O oxidation of SO_2 (Reaction R7), which is mass dependent (Ono et al., 2013).

At 5.1 kPa O_2 and above, elemental sulfur formation was shut off and SO_3 was the major product. Under these conditions, oxidation of SO (to SO_2 or SO_3 via Reactions R5 or R6) competes with SO disproportionation (Reaction R8).

By comparing the $\Delta^{33}S$ value of elemental sulfur in the absence of O_2 (0 kPa O_2) with the $\Delta^{33}S$ value of sulfate in the presence of O_2 (5.1 kPa to 19.8 kPa O_2), it is possible to estimate the fraction of sulfate formed through Reaction (R6). In particular,

$$f_{R6} = \frac{\Delta^{33}S_{\text{sulfate, with } O_2}}{\Delta^{33}S_{S^0,\ \text{no } O_2}} \quad (4)$$

where f_{R6} is the fraction of total SO_3 formed that comes from Reaction (R6). Given the product yields (Table 4), the time each experiment was run, and the volume of the reaction cell (approximately 325 cm^3), the sulfate formation rate per unit volume per unit time can be calculated. In the experiments with 5.1 kPa to 19.8 kPa O_2, the sulfate formation rates were between 5.3×10^{12} molecules $cm^{-3}\ s^{-1}$ and 1.2×10^{13} molecules $cm^{-3}\ s^{-1}$. Combining this with the f_{R6} values calculated from Eq. (5), we can estimate for the rate of sulfate formation from Reaction (R6) under our experimental conditions. This gave a rate for Reaction (R6) of 3.6×10^{12} molecules $cm^{-3}\ s^{-1}$

ACPD
14, 23499–23554, 2014

to 6.6×10^{12} molecules cm^{-3} s^{-1}. Assuming Reaction (R6) is a termolecular reaction, the rate for Reaction (R6) can be written as:

$$\text{rate R6} = k_{R6}[SO][O_2][M] \quad (5)$$

where k_{R6} is the termolecular rate constant for Reaction (R6) and [SO], [O_2] and [M] are the concentrations of SO, O_2 and total third body gases ($M = N_2$, O_2) in the reaction cell. In Eq. (6), the [O_2] and [M] terms are known from the experimental conditions. The [SO] term is estimated by assuming a photochemical steady state for SO in the cell. SO production via Reaction R4 is balanced by SO destruction via Reactions R5 and R6. This gives us a steady state SO concentration of:

$$[SO] = \frac{J_{SO_2}[SO_2]}{k_{R5}[O_2] + k_{R6}[O_2][M]} \quad (6)$$

where J_{SO_2} is the photolysis rate constant for reaction (R4). This photolysis rate constant was calculated assuming a spectral irradiance for our 150 W Xe arc lamp of:

$$F_0/\text{mW nm}^{-1} = 0.11 \cdot 1.6 \cdot (14 - 9 \cdot \exp(-0.013 \cdot (\lambda/\text{nm} - 200))) \quad (7)$$

where F_0 is the spectral irradiance of the xenon lamp at wavelength λ (Ono et al., 2013). The spectral irradiance was used to calculate the photon flux entering the cell, accounting for absorption of the cell windows from measured transmission data. The SO_2 absorption cross-sections of Manatt and Lane (1993) were used to calculate the photolysis rate in the cell, accounting for optical screening effects from SO_2 and O_2 within the cell. With an SO_2 partial pressure of 0.127 kPa, this provided a photolysis rate constant of $J_{SO_2} = 5.2 \times 10^{-3}$ s^{-1}. The rate constant for reaction R5 is $k_{R5} = 8.0 \times 10^{-17}$ cm^3 $molecule^{-1}$ s^{-1} (Sander et al., 2011) at room temperature (298 K). Using these values and Eqs. (6) and (7), the rate constant for Reaction (R6) (k_{R6}) was calculated iteratively. Calculated rate constants ranged from

ACPD
14, 23499–23554, 2014

$k_{R6} = 7.3 \times 10^{-38}$ cm^6 molecule^{-2} s^{-1} to $k_{R6} = 1.4 \times 10^{-37}$ cm^6 molecule^{-2} s^{-1}, with an average value of $k_{R6} = 1.1 \times 10^{-37}$ cm^6 molecule^{-2} s^{-1} (Table 4). This rate estimate is consistent with the upper bound on $k_{R6} \leq 1 \times 10^{-36}$ cm^6 molecule^{-2} s^{-1} by Black et al. (1982).

The derived rate constant carries a large amount of uncertainty due to a number of sources of error in the rate calculation. One source of error in the calculation is in the spectral irradiance of the xenon lamp, which was fit from the manufacturer's literature and not directly measured. Because the spectral irradiance is likely to change over the lamp's lifetime, the actual spectral irradiance at the time the experiments were performed might be different than the values calculated here. As the spectral irradiance in the high-energy side of the ultraviolet (190 to 220 nm) is likely to decrease over the course of the lamp's lifetime, this makes the calculated SO_2 photolysis rate (and resulting SO number density) an upper bound. Reducing the SO_2 photolysis rate increases the effective rate constant. A second source of error is the assumption that we trapped 100 % of the SO_3 formed as sulfate. It is possible that some fraction of the SO_3 remained in the gas phase and did not condense as aerosol particles. A third source of error is the assumption that the reaction R6 behaves as a termolecular reaction despite the high total pressure (101.3 kPa) of the system. It is possible that the reaction is saturated at (or near) this pressure and is thus behaving as an effective bimolecular reaction. In any of these three cases, the estimate of the rate constant for reaction R6 would be a lower bound on the actual termolecular rate constant.

4.4 Constraining the rate of the SO + O_2 + M reaction using a kinetic model

To further constrain the rate of Reaction (R6) (the SO + O_2 + M → SO_3 + M reaction), we constructed a kinetic model of the chemistry occurring within the cell. We used the same data and conditions as Sect. 4.3, but explicitly modeled the chemistry occurring within the system. SO_2 photolysis rates were calculated as discussed in Sect. 4.3, using the cross sections of Manatt and Lane (1993). Oxygen and ozone photolysis

ACPD
14, 23499–23554, 2014

rates were calculated using the cross-sections Yoshino et al. (1988, 1992) for O_2 and Molina and Molina (1986) for O_3. $O(^1D)$ formed from O_3 photolysis was assumed to be instantaneously quenched by N_2 and O_2 to $O(^3P)$ and not significantly affect the chemistry of the system.

Reactions considered, rate constants for those reactions, and the sources for the rate constants are given in Table 9. When possible, effective second-order rate constants (calculated assuming $T = 298$ K and $[M] = 2.5 \times 10^{19}$ molecule cm^{-3}) were used for termolecular reactions. Initial guesses were made for the concentration of species within the system. The system was assumed to be in photochemical steady state and solved iteratively until convergence. Comparisons were made between the data and the calculations for both f_{R6} values (Eq. 5) as well as total product (SO_3) formation rates. Simulations performed with values of k_{R6} between 1.0×10^{-37} cm^6 molecule^{-2} s^{-1} and 1.0×10^{-36} cm^6 molecule^{-2} s^{-1}. The observed f_{R6} value (Eq. 5) is best fit by the k_{R6} between 2×10^{-37} cm^6 molecule^{-2} s^{-1} and 10×10^{-37} cm^6 molecule^{-2} s^{-1} (Fig. 7, left). The yield of SO_3 indicates a lower rate constant of less than 1×10^{-37} cm^6 molecule^{-2} s^{-1} to 3×10^{-37} cm^6 molecule^{-2} s^{-1}, potentially reflecting low recovery of SO_3 in our experiments (Fig. 7, right). Nonetheless, this range of results is consistent with the rate estimate obtained in Sect. 4.3. Thus, our best estimate for the rate of reaction R6 is somewhere between 1.0×10^{-37} cm^6 molecule^{-2} s^{-1} and 1.0×10^{-36} cm^6 molecule^{-2} s^{-1}. As discussed in Sect. 4.3, the model is sensitive to the SO_2 photolysis rate, which depends upon the lamp spectrum.

4.5 Exploring the potential energy surfaces of the SO + O_2 reactions

The experimental evidence presented above suggests the formation of SO_3 via the $SO + O_2$ reaction. Our theoretical analysis shows that the singlet PES is associated with the ground state of the SO_3 molecule, and thus is the primary surface related to the $SO(^3\Sigma^-) + O_2(^3\Sigma_g^-) \rightarrow SO_3(^1A_1')$ reaction (Fig. 4). As shown in Table 7, four isomers of SO_3 are located in the singlet PES. It is predicted that the D_{3h} SO_3 molecule

ACPD
14, 23499–23554, 2014

is the global minimum, followed by the cyclic-OSOO. There are two shallow wells, denoted as trans-OSOO and cis-OSOO, at the CASPT2 and UCCSD(T)-F12a levels, but they seem to be energetically higher than the $SO(^3\Sigma^-) + O_2(^3\Sigma_g^-)$ asymptote at the B3LYP and CASSCF levels. No barrier was found for the formation of either trans-OSOO or cis-OSOO, but there is a barrier for the isomerization and the barrier height depends upon the level of the ab-initio calculation. The rate-determining barrier for the $SO(^3\Sigma^-) + O_2(^3\Sigma_g^-) \rightarrow SO_3(^1A_1')$ reaction is the one connecting the cyclic-OSOO and SO_3. The lowest barrier height for this reaction (given by CASPT2) is 56.6 kJ mole^{-1}. Using the partition function at the B3LYP level, a conventional transition-state theory rate calculation predicts a pressure-saturated (i.e. effective bimolecular) thermal rate constant for Reaction (R6) at 298 K of 2.7×10^{-24} cm^3 molecule^{-1} s^{-1}. This is about eight orders of magnitude lower than the experimental rate constant for Reaction (R5) (8.0×10^{-17} cm^3 molecule^{-1} s^{-1}, Sander et al., 2011), and about six orders of magnitude lower than the minimum effective second-order rate constant for reaction R6 at 101.3 kPa total pressure (about 2.5×10^{-18} cm^3 molecule^{-1} s^{-1}, calculated assuming $k_{R6} = 1.0 \times 10^{-37}$ cm^6 molecule^{-1} s^{-1} and [M] = 2.5×10^{19}). We thus conclude that the $SO(^3\Sigma^-) + O_2(^3\Sigma_g^-) \rightarrow SO_2(^1A_1) + O(^3P)$ reaction cannot occur on the singlet surface without invoking the spin-forbidden intersystem crossing between the singlet and triplet surfaces.

The triplet PES is very different from the singlet PES with regard to the energy of each SO_3 isomer (Fig. 4; Table 8). The global minimum moves to the cyclic-OSOO, which has a similar geometry to the singlet (ground) state counterpart but with different bond lengths. On the other hand, $SO_3(^3A_1')$ becomes highly unfavorable; for example, it is 75.14 kJ mole^{-1} higher than the $SO + O_2$ reactant at the UCCSD(T)-F12a level. The trans-OSOO complex remains in a planar geometry, in which the O-S-O-O dihedral angle is 180°; however, the cis-OSOO complex was found to be out-of-plane, in which the O-S-O-O dihedral angle is about 74°. We still use "cis-OSOO" to denote this isomer for convenience. Unlike the singlet PES, trans-OSOO and cis-OSOO share the same transition state for the isomerization to cyclic-OSOO. This process represents the rate-

ACPD
14, 23499–23554, 2014

limiting step for the reaction on the triplet surface. The barrier height is 67.86 kJ mole^{-1} at the UCCSD(T)-F12a level, which is still high. In the adiabatic picture, the $SO(^3\Sigma^-) + O_2(^3\Sigma_g^-) \rightarrow SO_2(^1A_1) + O(^3P)$ reaction on the triplet PES has a rate constant of 2.7×10^{-25} cm^3 molecule^{-1} s^{-1} at 298 K, estimated using transition-state theory. This is still considerably slower than the experimentally measured rate constant for Reaction (R5).

It is clear that a single PES is unable to reproduce the experimental data for Reactions (R5) and (R6). The deviation is rather large and cannot be attributed to tunneling effects. In order to explore the possibility of intersystem crossing, two adiabatic minimum energy pathways on both spin states are shown in Fig. 4 and the energies are extracted at the UCCSD(T)-F12a//B3LYP level. There are several places that the two PESs cross each other, and a spin flip could happen in the region near the cyclic-OSOO due to the fact that the cyclic-OSOO isomer on both PESs has nearly the same energy. A possible non-adiabatic reaction pathway is depicted in Fig. 4 by the green solid lines connecting every two stationary points. Specifically, for the $SO(^3\Sigma^-) + O_2(^3\Sigma_g^-) \rightarrow SO_3(^1A_1')$ reaction, the two reactants first approach each other to form cyclic-OSOO on the singlet PES, and jump to the triplet PES to avoid the high barrier region, followed by back transition to the singlet state to form the SO_3 product. For the $SO(^3\Sigma^-) + O_2(^3\Sigma_g^-) \rightarrow SO_2(^1A_1) + O(^3P)$ reaction, the intermediate cyclic-OSOO may be generated on the singlet PES, followed by intersystem crossing from the singlet to triplet surface and then reach the products without overcoming a high barrier. Indeed, several different mechanisms introduce the intersystem crossing have been proposed by other authors for the $SO_3 \rightarrow SO_2 + O$ reactions (Davis, 1974; Westenberg and Dehaas, 1975; Astholz et al., 1979), thanks to the relatively large spin-orbit coupling. The barrier associated with the intersystem crossing pathway seems to be consistent with the fast rate of Reaction (R5), and supports the facile formation of SO_3.

Unfortunately, rate constants involving the intersystem crossing cannot be readily determined without global PESs for both spin states and the coupling between them. Such a goal can only be achieved by a multi-reference method or configuration interaction method, which is infeasible at the current level.

ACPD
14, 23499–23554, 2014

4.6 Contribution of the $SO + O_2 + M$ reaction to sulfate formation in the stratosphere

To determine the significance of the Reaction (R6) to sulfate formation in the stratosphere, we compared the rate of sulfate formation via Reaction (R6) to that formed via OH oxidation of SO_2 (Reaction R1) and O oxidation of SO_2 (Reaction R7) under a select set of atmospheric conditions. We assumed an atmospheric temperature and pressure profile of the US Standard Atmosphere 1976 (COESA, 1976) and noon-time O, OH, and O_3 concentrations given by DeMore et al. (1997). Spectral photon flux in the 180 to 220 nm region was calculated as a function of altitude for a solar zenith angle of 40° by assuming the spectral photon irradiance of Rottman et al. (2006) at the top of the atmosphere and O_2, O_3, and CO_2 being the dominant absorbers. Absorption cross-sections of O_2 (Yoshino et al., 1988, 1992), O_3 (Molina and Molina, 1986), and CO_2 (Shemansky, 1972) were used with concentration and column density data for the species to calculate the transmission of the atmosphere to radiation in the 180 to 220 nm absorption region at different altitudes. SO_2 photolysis rate constants (J_{SO_2}) were calculated as a function of altitude using the calculated spectral photon fluxes and the SO_2 absorption cross-sections of Manatt and Lane (1993).

The lifetime of SO with respect to oxidation by O_2 (i.e. R5 and R6) is relatively short (on the order of seconds), so SO and SO_2 were assumed to be in photochemical steady state, i.e.

$$\frac{[SO]}{[SO_2]} = \frac{J_{SO_2}}{k_{R5}[O_2] + k_{R6}[O_2][M]} \quad (8)$$

The rate constant k_{R5} was calculated as a function of altitude (i.e. temperature) based on the recommendations of Sander et al. (2011). k_{R6} was varied between 1.0×10^{-37} cm^6 molecule^{-2} s^{-1} and 1.0×10^{-36} cm^6 molecule^{-2} s^{-1} to encompass our range of rate estimates from Sect. 4.3. SO oxidation by other oxidants (O_3, O, NO_3, etc.) was assumed to be minor compared to oxidation by O_2 given the minor concentration of most of these species compared with that of O_2. Using the [SO] to [SO_2] ratio,

ACPD
14, 23499–23554, 2014

the rates of Reactions (R1), (R7), and (R6) can be compared. Assuming these three reactions are the dominant source of SO_3 (and subsequently sulfate) in the stratosphere, the fraction of sulfate from Reaction (R6) (f_{SO}) can be calculated as:

$$f_{SO} = \frac{\frac{[SO]}{[SO_2]} \cdot k_{R6}[O_2][M]}{k_{SO_2+OH}[OH] + k_{SO_2+O}[O] + \frac{[SO]}{[SO_2]} \cdot k_{R6}[O_2][M]} \quad (9)$$

The rate constants k_{SO_2+OH} and k_{SO_2+O} are the effective bimolecular rate constants for Reactions (R1) and (R7), as recommended by Sander et al. (2011). f_{SO} values were calculated for a 40° solar zenith angle (local noon at 40° N latitude and a 0° solar declination angle) and are shown in Fig. 8. Given that SO, OH, and $O(^3P)$ are all formed as a result of photochemistry, they should have similar daily cycles. As a result, the f_{SO} values calculated for local noon should be similar to daily average f_{SO} values.

As seen in Fig. 8, the lower-bound estimate for k_{R6} (1.0×10^{-37} cm^6 molecule^{-2} s^{-1}) gives 4 % to 10 % of sulfate from Reaction (R6) between 25 km and 50 km altitude. A faster estimate for k_{R6} of 2.0×10^{-37} cm^6 molecule^{-2} s^{-1} gives 8 % to 18 % of sulfate from Reaction (R6) between 25 km and 50 km altitude. The upper bound estimate for the rate ($k_{R6} = 1.0 \times 10^{-36}$ cm^6 molecule^{-2} s^{-1}, from Black et al., 1982) suggests that over 45 % of sulfate could be coming from Reaction (R6) between 31 km and 34 km altitude and is probably unrealistic. The contribution from Reaction (R6) depends upon the amount of photons available for SO_2 photolysis, which increases with altitude because of less absorption by Schuman–Runge band of O_2 and the Hartley bands of O_3. The rate of Reaction (R6) decreases at higher altitude as total number density decrease. The maximum f_{SO} value, thus, is between 30 and 35 km (Fig. 8).

Some insight into the rate can be obtained from SO_2 lifetimes in the stratosphere. Following the Mt. Pinatubo (1991) eruption, the Total Ozone Mapping Spectrometer (TOMS) data (Bluth et al., 1992) and Microwave Limb Sounder (MLS) data (Read et al., 1993) were used to estimate an e-folding time of 33 days to 35 days for SO_2 in the stratosphere. A later reanalysis of the TOMS data and TIROS Optical Vertical

ACPD
14, 23499–23554, 2014

Sounder (TOVS) data (Guo et al., 2004) reduced this value to 25 days. Bekki and Pyle (1994) modeled the SO_2 decay following the Mt. Pinatubo eruption, considering Reaction (R1) as the only sink of SO_2 in the stratosphere. Their modeled decay times for SO_2 (40 days) are considerably longer than the measured value of 25 days. Bekki and Pyle (1994) attributed this to uncertainties in the OH number densities. The discrepancy, however, could be explained in part by SO_2 photolysis followed by Reaction (R6). Inclusion of the SO_2 photolysis sink would decrease the lifetimes for SO_2 above 25 km. The presence of this reaction would also suggest that OH concentrations estimated by Read et al. (1993) based on SO_2 lifetimes might overestimate OH concentrations above 25 km altitude.

SO_2 photolysis is self-limiting, as SO_2 photolysis near the top of the volcanic SO_2 plume absorbs ultraviolet radiation in the range that SO_2 photolysis occurs. As a result, SO_2 photolysis lower in the eruption cloud is reduced and depends upon the overlying SO_2 column density. This would potentially reduce the significance of R6 under heavy SO_2 loading.

Optical shielding effects increase the magnitude of the isotope effect from SO_2 photolysis under high SO_2 column densities (Lyons et al., 2007; Ono et al., 2013). Thus, the isotope fractionation occurring in a volcanic cloud is a tradeoff between larger fractionations but lower photolysis rates at higher column densities vs. smaller fractionations but higher photolysis rates at lower column densities. Although the instantaneous fractionation factors can be accurately estimated using our results and cross section by Lyons (2007, 2008), the temporal evolution of isotope signatures of sulfate aerosol will require a model that accurately incorporates both chemistry and dynamics of stratosphere.

Given the large signal produced by SO_2 photolysis, over 100 ‰ and 10 ‰ for $\delta^{34}S$ and $\Delta^{33}S$ values, respectively (Whitehill and Ono, 2012; Ono et al., 2013), even a 10 % contribution from Reaction (R5) could make a substantial contribution to the isotope signature of sulfate formed above circa 25 km altitude. Given the strong similarity in the isotopic signature of stratospheric sulfate aerosols from volcanic eruptions and those produced during SO_2 photolysis (Fig. 3), it is likely that SO_2 photolysis plays an

ACPD
14, 23499–23554, 2014

important role in the sulfur isotope budget of stratospheric sulfate aerosols. The initial sulfate formed from SO_2 photolysis (followed by R6) will contain positive $\delta^{34}S$ and $\Delta^{33}S$ values and negative $\Delta^{36}S$ values. Over time, due to mass balance, the residual SO_2 will obtain negative $\delta^{34}S$ and $\Delta^{33}S$ values and positive $\Delta^{36}S$ values. This explains the temporal evolution of the isotopic signatures observed in aerosol samples (for $\delta^{34}S$, Castleman et al., 1974) and ice cores (Baroni et al., 2007), which goes from positive $\delta^{34}S$ and $\Delta^{33}S$ values shortly after an eruption to negative values as time progresses.

4.7 Insignificance of excited-state photochemistry of SO_2 in the stratosphere

It has been suggested previously (Savarino et al., 2003; Hattori et al., 2013) that excited-state photochemistry of SO_2 in the 250 to 350 nm absorption region (i.e. the $\tilde{A}(^1A_2)/\tilde{B}(^1B_1)$ states) might be important to the sulfur isotope ratios in stratospheric sulfate aerosols. Previous results (Whitehill and Ono, 2012; Whitehill et al., 2013) have demonstrated that SO_2 photoexctiation in this region produces mass-independent sulfur isotope signatures with positive $\Delta^{36}S/\Delta^{33}S$ ratios, as opposed to the negative $\Delta^{36}S/\Delta^{33}S$ ratios measured for stratospheric sulfate aerosols. This study further demonstrates that SO_2 photoexcitation in the 250 to 350 nm absorption region produces positive $\Delta^{36}S/\Delta^{33}S$ ratios, even at temperatures approaching stratospheric temperatures. Our previous experiments (Whitehill and Ono, 2012; Whitehill et al., 2013) have been questioned as being inapplicable to the modern atmosphere (Hattori et al., 2013) due to the experimental conditions (i.e. the addition of C_2H_2 to trap triplet-state SO_2). In the present study, we tested SO_2 photoexcitation with two different longpass filters (250 nm longpass filter and 280 nm longpass filter) in a N_2/O_2 bath gas. In all cases, we produced sulfate products with positive $\Delta^{36}S/\Delta^{33}S$ ratios. Therefore, our experiments do not provide support for SO_2 photoexcitation as a source of the isotope anomalies in modern atmospheric samples.

ACPD
14, 23499–23554, 2014

4.8 Production and preservation of mass-independent sulfur isotope signatures in ice cores

The results presented in this paper can explain the production and preservation of mass-independent sulfur isotope signatures in the modern atmosphere. Large volcanic eruptions, such as Pinatubo (1991) and Agung (1963) inject large amounts of SO_2 into the stratosphere. Both direct injection into higher altitudes (i.e. above 25 km) or stratospheric transport of the SO_2 plume can bring SO_2 to a sufficient altitude for SO_2 photolysis to occur. The process of SO_2 photolysis produces large mass-independent sulfur isotope signatures in the SO products, particularly when there is high SO_2 loading (and thus optical screening effects). Reaction of SO with O_2 to produce SO_3 (via Reaction R6) provides a pathway for the isotopic signature of SO to be preserved as SO_3, which can subsequently form sulfate aerosols. Some portion of the sulfate aerosols containing the mass-independent sulfur isotope signatures are transported to polar regions, where they can be deposited in polar precipitation and preserved in ice core records. A schematic illustration of the process is shown in Fig. 9.

Some eruptions, despite their stratospheric influence, produce sulfate peaks in ice core records but do not contain mass-independent sulfur isotope signatures. Such eruptions include Cerro Hudson (1991, Savarino et al., 2003) and Laki (1783, Lanciki et al., 2012). Schmidt et al. (2012) discussed this issue previously and concluded that the Laki aerosols deposited in the Greenland ice cores were predominantly upper tropospheric or lower stratospheric in origin. Estimates for the height of the Laki (1783) eruption plume are only 15 km (Thordarson and Self, 2003), which penetrates the stratosphere but is not sufficiently high for SO_2 photolysis to be a dominant process (Schmidt et al., 2012). Due to the higher latitude of the eruption, transport processes are unlikely to bring the eruption plume to a sufficient altitude (25 km) for SO_2 photolysis to occur. Thus, despite the stratospheric influence of the Laki eruption, mass-independent sulfur isotope signatures in the preserved aerosols would not be expected. The situation is similar for the Cerro Hudson (1991) eruption, which had an injection

ACPD
14, 23499–23554, 2014

height of 11 km to 16 km (Schoeberl et al., 1993). Again, given the high latitude of the eruption, transport processes are likely insufficient to bring the plume above 25 km.

In contrast with this are major low-latitude eruptions such as Pinatubo (1991). Although the initial injection of the Pinatubo eruption was probably localized below 25 km, the evolution of the plume resulted in the plume reaching altitudes of 30 km or higher (Gobi et al., 1992), sufficient altitudes for SO_2 photolysis to play a role in the oxidation to sulfate. The largest mass-independent sulfur isotope signatures (with $\Delta^{33}S > 1$ ‰) observed to date are from the Samalas (1257, Lavigne et al., 2013) eruption (Lanciki et al., 2012). Evidence suggests the eruption plume from this reaction reached a minimum of 34 km altitude, with a likely estimate being 43 km altitude (Lavigne et al., 2013). At this altitude, SO_2 photolysis would become a dominant process, and could explain why the signature from this eruption is significantly larger that the other eruptions. Thus, SO_2 photolysis, followed by SO oxidation to SO_3 (via R6), presents a consistent mechanism through which mass-independent sulfur isotope signatures can be produced and preserved in the modern, oxygenated stratosphere.

5 Conclusions

Laboratory photochemical experiments were carried to investigate the production of mass-independent sulfur isotope effects under stratospheric conditions. For SO_2 photolysis in the 190 to 220 nm region, the magnitude of the mass-independent isotope signature increases with decreasing temperature. The isotope systematics, in particular $\delta^{34}S$ and $\Delta^{36}S$ values, show excellent agreement with an optical self-screening model based on synthetic absorption cross sections (Lyons, 2007). SO_2 photoexcitation experiments show similar signatures to previous experimental studies (Whitehill and Ono, 2012; Whitehill et al., 2013), with positive $\Delta^{33}S$ and $\Delta^{36}S$ values, but that differ significantly from expectations based on absorption cross sections (Danielache et al., 2012).

ACPD
14, 23499–23554, 2014

The SO_3 (recovered as sulfate) products from SO_2 photolysis in the presence of molecular oxygen carry mass-independent sulfur isotope signatures, suggesting a pathway for the direct oxidation of SO to SO_3. We hypothesize the $SO + O_2 + M \rightarrow SO_3 + M$ reaction (R6) and estimate the termolecular rate constant of the reaction to be on the order of 10^{-37} cm^6 molecule s^{-2} s^{-1}. This is consistent with previous constraints on the maximum rate of this reaction (Black et al., 1982).

We calculated the energies of stationary points on the singlet and triplet potential energy surfaces of SO_3 that are associated with the $SO(^3\Sigma^-) + O_2(^3\Sigma_g^-)$ asymptote at several different levels of theory and show that Reaction (R6) is theoretically possible via intersystem crossing between the singlet and triplet surfaces. We also show that the measured rate for $SO + O_2 + \rightarrow SO_2 + O$ reaction (R5) also requires intersystem crossing between the singlet and triplet surfaces.

Depending on the rate of Reaction (R6), we predict that on the order of 10 % of sulfate above 25 km altitude could be derived from the $SO + O_2 + M$ channel. Given the large isotope fractionations produced during SO_2 photolysis, our model can explain the source and preservation mechanism of mass-independent sulfur isotope signatures measured in stratospheric sulfate aerosols in polar ice samples. Our model explains the temporal evolution of $\delta^{34}S$ and $\Delta^{33}S$ values following major volcanic eruptions, and constrains the maximum altitude of the plume to 25 km and above when non-zero $\Delta^{33}S$ values are observed.

Acknowledgements. The authors would like to thank William J. Olszewski for his assistance in sulfur isotope analysis, and support from NASA Exobiology (NNX10AR85G to S.O., and 11-EXO11-0107 to H.G.) and NSF FESD (Award 1338810 to S.O.).

References

Ahmed, M. M.: Theoretical studies on the ground and excited states of SO_3 triatomic molecule, Chem. Sci. Trans., 2, 781–796, doi:10.7598/cst2013.515, 2013.

ACPD
14, 23499–23554, 2014

Astholz, D. C., Glanzer, K., and Troe, J.: The spin-forbidden dissociation-recombination reaction $SO_3 \rightarrow SO_2 + O$, J. Chem. Phys., 70, 2409–2413, doi:10.1063/1.437751, 1979.
Baroni, M., Thiemens, M. H., Delmas, R. J., and Savarino, J.: Mass-independent sulfur isotopic compositions in stratospheric volcanic eruptions, Science, 315, 84–87, doi:10.1126/science.1131754, 2007.
Baroni, M., Savarino, J., Cole-Dai, J., Rai, V. K., and Thiemens, M. H.: Anomalous sulfur isotope compositions of volcanic sulfate over the last millennium in Antarctic ice cores, J. Geophys. Res.-Atmos., 113, D20112, doi:10.1029/2008JD010185, 2008.
Becke, A. D.: Density-functional exchange-energy approximation with correct asymptotic behavior, Phys. Rev. A, 38, 3098–3100, doi:10.1103/PhysRevA.38.3098, 1988.
Becker, S., Braatz, C., Lindner, J., and Tiemann, E.: Investigation of the predissociation of SO_2: state selective detection of the SO and O fragments, Chem. Phys., 196, 275–291, doi:10.1016/0301-0104(95)00114-4, 1995.
Bekki, S.: Oxidation of volcanic SO_2: a sink for stratospheric OH and H_2O, Geophys. Res. Lett., 22, 913–916, doi:10.1029/95GL00534, 1995.
Bekki, S. and Pyle, J. A.: A two-dimensional modeling study of the volcanic eruption of Mount Pinatubo, J. Geophys. Res., 99, 18861–18869, doi:10.1029/94JD00667, 1994.
Black, G., Sharpless, R. L., and Slanger, T. G.: Rate coefficients at 298 K for SO reactions with O_2, O_3, and NO_2, Chem. Phys. Lett., 90, 55–58, doi:10.1016/0009-2614(82)83324-1, 1982.
Bluth, G. J. S., Doiron, S. D., Schnetzler, C. C., Krueger, A. J., and Walter, L. S.: Global tracking of the SO_2 clouds from the June 1991 Mount Pinatubo eruptions, Geophys. Res. Lett., 19, 151–154, doi:10.1029/91GL02792, 1992.
Canfield, D. E., Raiswell, R., Westrich, J. T., Reaves, C. M., and Berner, R. A.: The use of chromium reduction in the analysis of reduced inorganic sulfur in sediments and shales, Chem. Geol., 54, 149–155, doi:10.1016/0009-2541(86)90078-1, 1986.
Castleman, A. W., Munkelwitch, H. R., and Manowitz, B.: Isotopic studies of the sulfur component of the stratospheric aerosol layer, Tellus, 26, 222–234, doi:10.1111/j.2153-3490.1974.tb01970.x, 1974.
Celani, P. and Werner, H.-J.: Multireference perturbation theory for large restricted and selected active space reference wave functions, J. Chem. Phys., 112, 5546–5557, doi:10.1063/1.481132, 2000.
Chase, M. W., Davies, C. A., Downey, J. R., Frurip, D. J., McDonald, R. A., and Syverud, A. N.: Nist Janaf Thermochemical Tables 1985 Version 1.0, Standard Reference Data Program, Na-

ACPD
14, 23499–23554, 2014

tional Institute of Standards and Technology, Gaithersburg, MD, available at: http://kinetics.nist.gov/janaf/ (last access: 5 September 2014), 1986.
Chung, K., Calvert, J. G., and Bottenheim, J. W.: The photochemistry of sulfur dioxide excited within its first allowed band (3130 Å) and the "forbidden" band (3700–4000 Å), Int. J. Chem. Kinet., 7, 161–182, doi:10.1002/kin.550070202, 1975.
Cobos, C. J., Hippler, H., and Troe, J.: Falloff curves of the recombination reaction $O + SO + M \rightarrow SO_2 + M$ in a variety of bath gases, J. Phys. Chem., 89, 1778–1783, doi:10.1021/j100255a048, 1985.
COESA (Committee on Extension to the Standard Atmosphere): US Standard Atmosphere, 1976, US Government Printing Office, Washington, DC, USA, 1976.
Danielache, S. O., Eskebjerg, C., Johnson, M. S., Ueno, Y., and Yoshida, N.: High-precision spectroscopy of ^{32}S, ^{33}S, and ^{34}S sulfur dioxide: ultraviolet absorption cross sections and isotope effects, J. Geophys. Res.-Atmos., 113, D17314, doi:10.1029/2007JD009695, 2008.
Danielache, S. O., Hattori, S., Johnson, M. S., Ueno, Y., Nanbu, S., and Yoshida, N.: Photoabsorption cross-section measurements of ^{32}S, ^{33}S, ^{34}S, and ^{36}S sulfur dioxide for the B^1B_1–X^1A_1 absorption band, J. Geophys. Res.-Atmos., 117, D24301, doi:10.1029/2012JD017464, 2012.
Davis, D. D.: A kinetics review of atmospheric reactions involving H_xO_y compounds, Can. J. Chem., 52, 1405–1414, doi:10.1139/v74-213, 1974.
DeMore, W. B., Sander, S. P., Golden, D. M., Hampson, R. F., Kurylo, M. J., Howard, C. J., Ravishankara, A. R., Kolb, C. E., and Molina, M. J.: Chemical Kinetics and Photochemical Data For Use in Stratospheric Modeling, Evaluation Number 12, JPL Publication 97-4, Jet Propulsion Laboratory, Pasadena, California, USA, 1997.
Dunning, T. H.: Gaussian basis sets for use in correlated molecular calculations. I. The atoms boron through neon and hydrogen, J. Chem. Phys., 90, 1007–1023, doi:10.1063/1.456153, 1989.
Forrest, J. and Newman, L.: Silver-110 microgram sulfate analysis for the short time resolution of ambient levels of sulfur aerosol, Anal. Chem., 49, 1579–1584, doi:10.1021/ac50019a030, 1977.
Freeman, D. E., Yoshino, K., Esmond, J. R., and Parkinson, W. H., High resolution absorption cross section measurements of SO_2 at 213 K in the wavelength region 172–240 nm, Planet. Space Sci., 32, 1125–1134, doi:10.1016/0032-0633(84)90139-9, 1984.

ACPD
14, 23499–23554, 2014

Frisch, M. J., Trucks, G. W., Schlegel, H. B., Scuseria, G. E., Robb, M. A., Cheeseman, J. R., Scalmani, G., Barone, V., Mennucci, B., Petersson, G. A., Nakatsuji, H., Caricato, M., Li, X., Hratchian, H. P., Izmaylov, A. F., Bloino, J., Zheng, G., Sonnenberg, J. L., Hada, M., Ehara, M., Toyota, K., Fukuda, R., Hasegawa, J., Ishida, M., Nakajima, T., Honda, Y., Kitao, O., Nakai, H., Vreven, T., Montgomery, J. A., Jr.; Peralta, J. E., Ogliaro, F., Bearpark, M., Heyd, J. J., Brothers, E., Kudin, K. N., Staroverov, V. N., Kobayashi, R., Normand, J., Raghavachari, K., Rendell, A., Burant, J. C., Iyengar, S. S., Tomasi, J., Cossi, M., Rega, N., Millam, M. J., Klene, M., Knox, J. E., Cross, J. B., Bakken, V., Adamo, C., Jaramillo, J., Gomperts, R., Stratmann, R. E., Yazyev, O., Austin, A. J., Cammi, R., Pomelli, C., Ochterski, J. W., Martin, R. L., Morokuma, K., Zakrzewski, V. G., Voth, G. A., Salvador, P., Dannenberg, J. J., Dapprich, S., Daniels, A. D., Farkas, Ö., Foresman, J. B., Ortiz, J. V., Cioslowski, J., Fox, D. J.: Gaussian 09, Gaussian, Inc., Wallingford, CT, available at: http://www.gaussian.com/ (last access: 5 September 2014), 2009.

Gobbi, G. P., Congeduti, F., and Adriani, A.: Early stratospheric effects of the Pinatubo eruption, Geophys. Res. Lett., 19, 997–1000, doi:10.1029/92GL01038, 1992.

Goodarzi, M., Vahedpour, M., and Nazari, F.: Theoretical study on the atmospheric formation of SO_x ($x = 1 - 3$) in the SSO(^{1}A′) and $O_2(^3\Sigma_g^-)$ reaction, J. Molec. Struct. Theochem., 945, 45–52, doi:10.1016/j.theochem.2010.01.004, 2010.

Guo, S., Bluth, G. J. S., Rose, W. I., Watson, I. M., Prata, A. J.: Re-evaluation of SO_2 release of the 15 June 1991 Pinatubo eruption using ultraviolet and infrared satellite sensors, Geochem. Geophy. Geosy., 5, Q04001, doi:10.1029/2003GC000654, 2004.

Harris, E., Sinha, B., Hoppe, P., Crowley, J. N., Ono, S., and Foley, S.: Sulfur isotope fractionation during oxidation of sulfur dioxide: gas-phase oxidation by OH radicals and aqueous oxidation by H_2O_2, O_3 and iron catalysis, Atmos. Chem. Phys., 12, 407–423, doi:10.5194/acp-12-407-2012, 2012.

Harris, E., Sinha, B., Hoppe, P., and Ono, S.: High-precision measurements of ^{33}S and ^{34}S fractionation during SO_2 oxidation reveal causes of seasonality in SO_2 and sulfate isotopic composition, Environ. Sci. Technol., 47, 12174–12183, doi:10.1021/es402824c, 2013.

Hattori, S., Schmidt, J., Johnson, M. S., Danielache, S. O., Yamada, A., Ueno, Y., and Yoshida, N.: SO_2 phootoexcitation mechanism links mass-independent sulfur isotopic fractionation in cryospheric sulfate to climate impacting volcanism, P. Natl. Acad. Sci. USA, 110, 17656–17661, doi:10.1073/pnas.1213153110, 2013.

ACPD
14, 23499–23554, 2014

Jou, S. H., Shen, M. Y., Yu, C. H., and Lee, Y. P.: Isomers of SO_3: infrared absorption of OSOO in solid argon, J. Chem. Phys., 104, 5745–5753, doi:10.1063/1.471335, 1996.

Katagiri, H., Sako, T., Hishikawa, A., Yazaki, T., Onda, K., Yamanouchi, K., and Yoshino, K.: Experimental and theoretical exploration of photodissociation of SO_2 via the C^1B_2 state: identification of the dissociation pathway, J. Molec. Struct., 413, 589–614, doi:10.1016/S0022-2860(97)00199-3, 1997.

Knizia, G., Adler, T. B., and Werner, H.-J.: Simplified CCSD(T)-F12 methods: theory and benchmarks, J. Chem. Phys., 130, 054104, doi:10.1063/1.3054300, 2009.

Knowles, P. J. and Werner, H.-J.: An efficient second-order MC SCF method for long configuration expansions, Chem. Phys. Lett., 115, 259–267, doi:10.1016/0009-2614(85)80025-7, 1985.

Knowles, P. J. and Werner, H.-J.: An efficient method for the evaluation of coupling coefficients in configuration interaction calculations, Chem. Phys. Lett., 145, 514–522, doi:10.1016/0009-2614(88)87412-8, 1988.

Lanciki, A. L.: Discovery of Sulfur Mass-Independent Fractionation (MIF) Anomaly of Stratospheric Volcanic Eruptions in Greenland Ice Cores, Ph. D. thesis, South Dakota State University, Brookings, South Dakota, USA, 141 pp., 2010.

Lanciki, A., Cole-Dai, J., Thiemens, M. H., and Savarino, J.: Sulfur isotope evidence of little or no stratospheric impact by the 1783 Laki volcanic eruption, Geophys. Res. Lett., 39, L01806, doi:10.1029/2011GL050075, 2012.

Lavigne, F., Degeai, J. P., Komorowski, J. C., Guillet, S., Robert, V., Lahitte, P., Oppenheimer, C., Stoffel, M., Vidal, C. M., Surono, Pratomo, I., Wassmer, P., Hajdas, I., Hadmoko, D. S., and Belizal, E.: Source of the great A. D. 1257 mystery eruption unveiled, Samalas volcano, Rinjani Volcanic Complex, Indonesia, P. Natl. Acad. Sci. USA, 110, 16742–16747, doi:10.1073/pnas.1307520110, 2013.

Lee, C., Yang, W., and Parr, R. G., Development of the Colle–Salvetti correlation-energy formula into a functional of electron density, Phys. Rev. B, 37, 785–789, doi:10.1103/PhysRevB.37.785, 1988.

Leung, F., Colussi, A. J., and Hoffmann, M. R.: Sulfur isotopic fractionation in the gas-phase oxidation of sulfur dioxide initiated by hydroxyl radicals, J. Phys. Chem. A, 105, 8073–8076, doi:10.1021/jp011014+, 2001.

ACPD
14, 23499–23554, 2014

Lévêque, C., Taïeb, R., and Köppel, H.: Communication: theoretical prediction of the importance of the $^3B_2$ state in the dynamics of sulfur dioxide, J. Chem. Phys., 140, 091101, doi:10.1063/1.4867252, 2014.
Lyons, J. R.: Mass-independent fractionation of sulfur isotopes by isotope-selective photodissociation of SO_2, Geophys. Res. Lett., 34, L22811, doi:10.1029/2007GL031031, 2007.
Lyons, J. R.: Photolysis of long-lived predissociative molecules as a source of mass-independent isotope fractionation: the example of SO_2, Adv. Quant. Chem., 55, 57–74, doi:10.1016/S0065-3276(07)00205-5, 2008.
Manatt, S. L. and Lane, A. L.: A compilation of the absorption cross-sections of SO_2 from 106 to 403 nm, J. Quant. Spectrosc. Ra., 50, 267–276, doi:10.1016/0022-4073(93)90077-U, 1993.
Martin, J. M. L.: Heat of atomization of sulfur trioxide, SO_3: a benchmark for computational thermochemistry, Chem. Phys. Lett., 310, 271–276, doi:10.1016/S0009-2614(99)00749-6, 1999.
Masterson, A. L., Farquhar, J., and Wing, B. A.: Sulfur mass-independent fractionation patterns in the broadband UV photolysis of sulfur dioxide: pressure and third body effects, Earth Planet. Sc. Lett., 306, 253–260, doi:10.1016/j.epsl.2011.04.004, 2011.
Molina, L. T. and Molina, M. J.: Absolute absorption cross sections of ozone in the 185- to 350-nm wavelength range, J. Geophys. Res.-Atmos., 91, 14501–14501, doi:10.1029/JD091iD13p14501, 1986.
Oduro, H., Kamyshny Jr, A., Guo, W., and Farquhar, J.: Multiple sulfur isotope analysis of volatile organic sulfur compounds and their sulfonium precursors in coastal marine environments, Mar. Chem., 124, 78–89, doi:10.1016/j.marchem.2010.12.004, 2011.
Ono, S., Whitehill, A. R., and Lyons, J. R.: Contribution of isotopologue self-shielding to sulfur mass-independent fractionation during sulfur dioxide photolysis, J. Geophys. Res.-Atmos., 118, 2444–2454, doi:10.1002/jgrd.50183, 2013.
Pavlov, A. A., Mills, M. J., and Toon, O. B.: Mystery of the volcanic mass-independent sulfur isotope fractionation signature in the Antarctic ice core, Geophys. Res. Lett., 32, L12816, doi:10.1029/2005GL022784, 2005.
Ran, H., Xie, D., and Guo, H.: Theoretical studies of the C^1B_2 absorption spectra of SO_2 isotopomers, Chem. Phys. Lett., 439, 280–283, doi:10.1016/j.cplett.2007.03.103, 2007.
Read, W. G., Froidevaux, L., and Waters, J. W.: Microwave limb sounder measurement of stratospheric SO_2 from the Mt. Pinatubo Volcano, Geophys. Res. Lett., 20, 1299–1302, doi:10.1029/93GL00831, 1993.

ACPD
14, 23499–23554, 2014

Robock, A.: Volcanic eruptions and climate, Rev. Geophys., 38, 191–219, doi:10.1029/1998RG000054, 2000.
Rottman, G. J., Woods, T. N., and McClintock, W.: SORCE solar UV irradiance results, Adv. Space Res., 37, 201–208, doi:10.1016/j.asr.2005.02.072, 2006.
Sander, S. P., Abbatt, J., Barker, J. R., Burkholder, J. B., Friedl, R. R., Golden, D. M., Huie, R. E., Kolb, C. E., Kurylo, M. J., Moortgat, G. K., Orkin, V. L., and Wine, P. H.: Chemical Kinetics and Photochemical Data For Use in Atmospheric Studies, Evaluation No. 17, JPL Publication 10-6, Jet Propulsion Laboratory, Pasadena, California, USA, available at: http://jpldataeval.jpl.nasa.gov/ (last access: 5 September 2014), 2011.
Savarino, J., Romero, J., Cole-Dai, J., Bekki, S., and Thiemens, M. H.: UV induced mass-independent sulfur isotope fractionation in stratospheric volcanic sulfate, Geophys. Res. Lett., 30, 2131, doi:10.1029/2003GL018134, 2003.
Schmidt, A., Thordarson, T., Oman, L. D., Robock, A., and Self, S.: Climatic impact of the long-lasting 1783 Laki eruption: inapplicability of mass-independent sulfur isotopic composition measurements, J. Geophys. Res., 117, D23116, doi:10.1029/2012JD018414, 2012.
Schoeberl, M. R., Doiron, S. D., Lait, L. R., Newman, P. A., and Krueger, A. J.: A simulation of the Cerro Hudson SO_2 cloud, J. Geophys. Res., 98, 2949–2955, doi:10.1029/92JD02517, 1993.
Shemansky, D. E.: CO_2 extinction coefficient 1700–3000A, J. Chem. Phys., 56, 1582, doi:10.1063/1.1677408, 1972.
Tanaka, N., Rye, D. M., Xiao, Y., and Lasaga, A. C.: Use of stable sulfur isotope systematics for evaluating oxidation reaction pathways and in-cloud scavenging of sulfur-dioxide in the atmosphere, Geophys. Res. Lett., 21, 1519–1522, doi:10.1029/94GL00893, 1994.
Thordarson, T. and Self, S.: Atmospheric and environmental effects of the 1783–1784 Laki eruption: a review and reassessment, J. Geophys. Res., 108, 4011, doi:10.1029/2001JD002042, 2003.
Tokue, I. and Nanbu, S.: Theoretical studies of absorption cross sections for the C^1B_2-X^1A_1 system of sulfur dioxide and isotope effects, J. Chem. Phys., 132, 024301, doi:10.1063/1.3277191, 2010.
Werner, H.-J., Knowles, P. J., Knizia, G., Manby, F. R., Schütz, M, Celani, P., Korona, T., Lindh, R., Mitrushenkov, A., Rauhut, G., Shamasundar, K. R., Adler, T. B., Amos, R. D., Bernhardsson, A., Berning, A., Cooper, D. L., Deegan, M. J. O., Dobbyn, A. J., Eckert, F., Goll, E., Hampel, C., Hesselmann, A., Hetzer, G., Hrenar, T., Jansen, G., Köppl, C., Liu, Y.,

ACPD
14, 23499–23554, 2014

Lloyd, A. W., Mata, R. A., May, A. J., McNicholas, S. J., Meyer, W., Mura, M. E., Nicklass, A., O'Neill, D. P., Palmieri, P., Peng, D., Pflüger, K., Pitzer, R., Reiher, M., Shiozaki, T., Stoll, H., Stone, A. J., Tarroni, R., Thorsteinsson, T., and Wang, M.: MOLPRO, version 2012.1, a Package of ab initio Programs, Cardiff, UK, available at: http://www.molpro.net (last access: 5 September 2014), 2012.

Westenberg, A. A. and Dehaas, N.: Rate of the O + SO_3 reaction, J. Chem. Phys., 62, 725–730, doi:10.1063/1.430477, 1975.

Whitehill, A. R. and Ono, S.: Excitation band dependence of sulfur isotope mass-independent fractionation during photochemistry of sulfur dioxide using broadband light sources, Geochim. Cosmochim. Ac., 94, 238–253, doi:10.1016/j.gca.2012.06.014, 2012.

Whitehill, A. R., Xie, C., Hu, X., Xie, D., Guo, H., and Ono, S.: Vibronic origin of sulfur mass-independent isotope effect in photoexcitation of SO_2 at the implications to the early earth's atmosphere, P. Natl. Acad. Sci. USA, 110, 17697–17702, doi:10.1073/pnas.1306979110, 2013.

Xie, C., Hu, X., Zhou, L., Xie, D., and Guo, H.: Ab initio determination of potential energy surfaces for the first two UV absorption bands of SO_2, J. Chem. Phys., 139, 014305, doi:10.1063/1.4811840, 2013.

Yoshino, K., Cheung, A. S. C., Esmond, J. R., Parkinson, W. H., Freeman, D. E., Guberman, S. L., Jenouvrier, A., Coquart, B., and Merienne, M. F.: Improved absorption cross-sections of oxygen in the wavelength region 205–240 nm of the Herzberg continuum, Planet. Space Sci., 36, 1469–1475, doi:10.1016/0032-0633(88)90012-8, 1988.

Yoshino, K., Esmond, J. R., Cheung, A. S. C., Freeman, D. E., and Parkinson, W. H.: High resolution absorption cross sections in the transmission window of the Schumann–Runge bands and Herzberg continuum of O_2, Planet. Space Sci., 40, 185–192, doi:10.1016/0032-0633(92)90056-T, 1992.

ACPD
14, 23499–23554, 2014

Table 1. Summary of experiments performed.

Experiment	Lamp	Filter	T/K	Bath Gas	Presented in
photolysis (temp.)	200 W D_2	None	225 to 275	N_2	Figs. 2 and 5; Table 2
photoexcitation (temp.)	150 W Xe	250 LP, H_2O	225 to 275	N_2/C_2H_2	Fig. 2; Table 3
photolysis (added O_2)	150 W Xe	None, 200 BP	298	N_2/O_2	Figs. 3 and 6; Tables 4, 5
photoexcitation (added O_2)	150 W Xe	250 LP, 280 LP	298	N_2/O_2	Fig. 3; Table 5

ACPD
14, 23499–23554, 2014

Table 2. Isotope ratios of elemental sulfur products from the SO_2 photolysis temperature experiments (Sect. 2.2).

T/K	δ^{33}S/‰	δ^{34}S/‰	δ^{36}S/‰	Δ^{33}S/‰	Δ^{36}S/‰
225	103.05	191.16	349.12	8.02	−32.4
225	97.85	177.76	315.71	9.13	−35.8
250	87.19	161.31	288.97	6.61	−29.8
250	80.68	146.58	259.31	7.18	−28.9
275	72.16	132.59	236.37	5.57	−24.1
275	70.35	129.04	227.26	5.50	−25.5

ACPD
14, 23499–23554, 2014

Table 3. Isotope ratios of organosulfur products from the SO_2 photoexcitation temperature experiments (Sect. 2.2).

T/K	δ^{33}S/‰	δ^{34}S/‰	δ^{36}S/‰	Δ^{33}S/‰	Δ^{36}S/‰
225	24.18	9.88	65.72	19.01	46.0
225	24.94	9.95	67.09	19.73	47.2
250	25.29	7.33	64.39	21.44	49.7
250	24.30	6.37	62.38	20.96	49.6
275	26.24	5.39	63.29	23.4	52.5
275	25.39	4.84	61.27	22.84	51.6

ACPD
14, 23499–23554, 2014

Table 4. Results from experiments of SO_2 photolysis in the presence of varying amounts of O_2 (Sect. 2.3) used to estimate k_{R6} (Sects. 4.3 and 4.4).

Product	pO_2/ kPa	Time/ ks	Yield/ µmol S	$\delta^{33}S$/ ‰	$\delta^{34}S$/ ‰	$\delta^{36}S$/ ‰	$\Delta^{33}S$/ ‰	$\Delta^{36}S$/ ‰	calculated k_{R6}/ $cm^6\ molecule^{-2}\ s^{-1}$
* $S^0 - 1$	0.00	21.6		74.00	129.68	220.54	8.63	−31.9	
* $S^0 - 2$	0.00	21.6		78.42	137.52	232.90	9.18	−34.8	
S^0 avg	0.00						8.91	−33.3	
* $SO_3 - 1$	0.00	21.6	35.3	14.16	25.64	43.82	1.02	−5.2	
* $SO_3 - 2$	0.00	21.6	28.9	11.51	21.14	36.21	0.67	−4.2	
SO_3	5.07	7.2	46.0	45.47	79.75	134.34	4.97	−19.5	1.4×10^{-37}
SO_3	5.07	7.2	32.6	50.85	89.24	150.93	5.59	−21.6	1.1×10^{-37}
SO_3	10.13	7.2	37.1	51.60	90.27	151.99	5.82	−22.5	1.3×10^{-37}
SO_3	10.13	7.2	41.3	51.35	91.22	155.00	5.13	−21.5	1.3×10^{-37}
SO_3	15.20	7.2	37.4	51.43	89.67	150.68	5.94	−22.6	1.3×10^{-37}
SO_3	15.20	7.2	20.8	55.14	97.09	164.55	5.97	−23.4	7.3×10^{-38}
SO_3	19.75	10.8	40.4	53.18	94.68	161.22	5.24	−22.2	8.3×10^{-38}
SO_3	19.75	10.8	39.1	54.18	96.59	164.45	5.29	−22.7	8.1×10^{-38}

* $S^0 - 1$ and $SO_3 - 1$ are elemental sulfur and SO_3 from the same experiment. Similarly, $S^0 - 2$ and $SO_3 - 2$ are elemental sulfur and SO_3 from the same experiment.

ACPD
14, 23499–23554, 2014

Table 5. Results from additional experiments of SO_2 photolysis in the presence of O_2 (Sect. 2.3). All results are from sulfate (SO_3) product. Experiments were performed at a constant total pressure of 101.3 kPa unless marked otherwise. Filter types are: 200 BP = 200 nm bandpass filter, 250 LP = 250 nm longpass filter, 280 LP = 280 nm longpass filter.

Filter	pSO_2/ Pa	pO_2/ kPa	Flow/ $cm^3\ s^{-1}$	Time/ ks	Yield/ µmol S	$\delta^{33}S$/ ‰	$\delta^{34}S$/ ‰	$\delta^{36}S$/ ‰	$\Delta^{33}S$/ ‰	$\Delta^{36}S$/ ‰
none	314.0	19.00	16.67	1.8	62.3	38.45	67.23	117.84	4.22	−12.2
none	316.6	18.99	6.67	12.8	105.7	34.71	60.89	104.88	3.69	−12.5
none	50.7	20.06	1.67	18.0	70.9	32.91	58.18	95.36	3.26	−16.2
none	50.7	20.06	1.67	10.8	41.8	37.46	67.09	112.12	3.34	−17.0
none	25.2	20.16	1.68	18.0	40.8	22.80	40.08	64.63	2.31	−12.0
none	25.2	20.16	1.68	10.8	19.3	19.59	35.15	58.01	1.61	−9.2
* none	349.9	0.20	0.29	19.8	34.0	34.02	59.04	104.90	3.92	−9.2
200 BP	316.6	18.99	6.67	67.8	86.2	47.67	89.15	162.21	2.59	−11.9
200 BP	50.7	20.06	1.67	36.0	–	35.65	65.22	111.79	2.50	−14.0
250 LP	506.5	18.23	1.67	61.2	14.9	9.40	15.97	32.53	1.19	1.9
250 LP	506.5	18.23	1.67	61.2	1.9	19.56	33.12	68.70	2.60	4.5
280 LP	316.6	18.99	6.67	86.4	6.7	3.22	4.25	9.34	1.03	1.2

* Experiment performed at 7.7 kPa total pressure to test low pressure limit.

ACPD
14, 23499–23554, 2014

Table 6. Comparison of asymptotic energies of $SO + O_2$ obtained on the singlet and triplet potential energy surfaces for SO_3 and those obtained by the sum of two separated species. All energies are in kJ mole^{-1} and are relative to the $SO(^3\Sigma^-) + O_2(^3\Sigma_g^-)$ calculated separately in each ab-initio method.

	B3LYP	CASSCF	CASPT2//CASSCF	UCCSD(T)F12a//B3LYP
$SO(^3\Sigma^-) + O_2(^3\Sigma_g^-)$ (separated)	0	0	0	0
$SO(^1\Delta) + O_2(^3\Sigma_g^-)$ (separated)	118.78	64.60	136.36	94.98
$SO(^3\Sigma^-) + O_2(^1\Delta_g)$ (separated)	160.83	86.57	98.28	121.55
$SO(^1\Delta) + O_2(^1\Delta_g)$ (separated)	279.57	151.17	234.64	216.48
$SO + O_2$ (singlet)	279.57	0.00	−6.86	217.19
$SO + O_2$ (triplet)	27.61	0.00	−6.61	122.59

ACPD
14, 23499–23554, 2014

Table 7. Energies for stationary points on the singlet state potential energy surface at various ab-initio levels. The energy is relative to the $SO(^3\Sigma^-)+O_2(^3\Sigma_g^-)$ asymptote and zero point energy is not included. All energies are given in kJ mole^{-1}.

	B3LYP	CASSCF	CASPT2//CASSCF	UCCSD(T)F12a//B3LYP
SO_3	−287.73	−262.92	−348.69	−411.58
cyclic-OSOO	−60.17	−50.21	−101.75	−142.72
trans-OSOO	42.09	53.72	−18.87	−17.66
cis-OSOO	19.33	35.82	−31.42	−39.08
TS1: trans-to-cis	108.95	135.14	66.32	42.76
TS2: trans-to-cyclic	62.51	69.71	3.10	0.17
TS3: cis-to-cyclic	108.95	114.18	50.42	43.26
TS4: cyclic-to-SO_3	82.42	69.25	56.61	70.33
$SO(^3\Sigma^-) + O_2(^3\Sigma_g^-)$	0.00	0.00	0.00	0.00
$SO_2(^1A_1) + O(^1D)$	292.04	159.28	206.27	152.84

ACPD
14, 23499–23554, 2014

Table 8. Energies for stationary points on the triplet state potential energy surface at various ab-initio levels. The energy is relative to the $SO(^3\Sigma^-)+O_2(^3\Sigma_g^-)$ asymptote and zero point energy is not included. All energies are given in kJ mole^{-1}.

	B3LYP	CASSCF	CASPT2//CASSCF	UCCSD(T)F12a//B3LYP
SO_3	136.02	293.21	115.90	75.14
cyclic-OSOO	−70.67	12.18	−105.06	−137.07
trans-OSOO	26.40	85.81	8.70	16.53
cis-OSOO	28.58	82.09	16.82	18.49
TS1: trans-to-cis	30.42	92.72	10.79	25.44
TS2: OSOO-to-cyclic	96.40	125.35	67.28	67.86
$SO_2 \ldots O$	23.35	−71.34	−31.55	−58.28
TS3: cyclic-to-$SO_2 \ldots O$	25.44	−62.93	−24.81	−54.06
$SO(^3\Sigma^-) + O_2(^3\Sigma_g^-)$	0.00	0.00	0.00	0.00
$SO_2(^1A_1) + O(^3P)$	26.69	−55.44	13.64	−52.93

ACPD
14, 23499–23554, 2014

Table 9. Reactions and rate constants included in the kinetic model of the chemistry occurring within reaction cell. Rate constants have units of s^{-1} for first order reactions, cm^3 $molecule^{-1}$ s^{-1} for second order reactions (and effective second order reactions), and cm^6 $molecule^{-2}$ s^{-1} for third order reactions.

Reaction Number	Reaction	Rate constant	Reaction Order	Source
Photochemical Reactions				
R4	$SO_2 + h\nu \rightarrow SO + O$	5.2×10^{-3}	1	Manatt and Lane (1993)
R9	$O_2 + h\nu \rightarrow O + O$	1.7×10^{-6}	1	Yoshino et al. (1988, 1992)
R10	$O_3 + h\nu \rightarrow O + O_2$	1.1×10^{-1}	1	Molina and Molina (1986)
O_x Chemistry				
R11	$O + O + M \rightarrow O_2 + M$	1.0×10^{-33}	3	Sander et al. (2011)
R12	$O + O_2 + M \rightarrow O_3 + M$	6.0×10^{-34}	3	Sander et al. (2011)
R13	$O + O_3 \rightarrow O_2 + O_2$	8.0×10^{-15}	2	Sander et al. (2011)
SO_x Chemistry				
R5	$SO + O_2 \rightarrow SO_2 + O$	8.0×10^{-11}	2	Sander et al. (2011)
R6	$SO + O_2 + M \rightarrow SO_3 + M$	Varies	3	
R7	$SO_2 + O + M \rightarrow SO_3 + M$	1.3×10^{-14}	*2	Sander et al. (2011)
R8	$SO + SO \rightarrow SO_2 + S$	8.3×10^{-16}	2	Chung et al. (1975)
R14	$SO + O + M \rightarrow SO_2 + M$	1.3×10^{-11}	*2	Cobos et al. (1985)
R15	$SO + O_3 \rightarrow SO_2 + O_2$	8.4×10^{-14}	2	Sander et al. (2011)
R16	$S + O_2 \rightarrow SO + O$	2.3×10^{-12}	2	Sander et al. (2011)
R17	$S + O_3 \rightarrow SO + O_2$	1.2×10^{-11}	2	Sander et al. (2011)
Other				
k_out	Exit rate from cell	2.1×10^{-2}	1	

* Effective second order reactions based on falloff curves for [M] = 2.5×10^{19} and M = N_2, O_2. See sources for additional information.

ACPD
14, 23499–23554, 2014

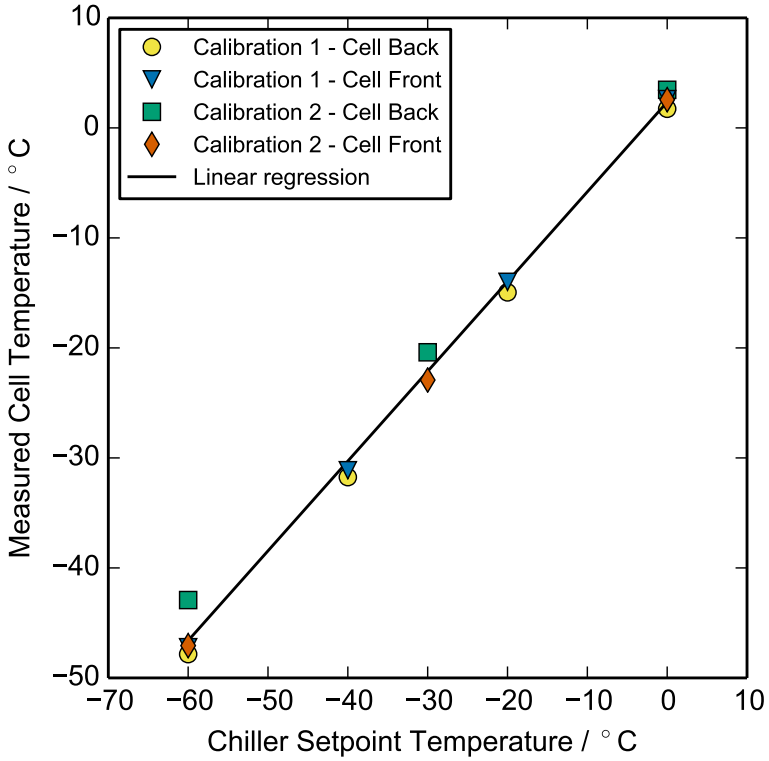

Figure 1. Results of the temperature calibration for the temperature controlled photochemical reactor described in Sect. 2.1 The linear regression shown was used to calibrate the temperature within the cell based on the setpoint temperature of the chiller. The regression line is $(T_{Cell}/^{\circ}C) = 0.8160 \times (T_{Chiller}/^{\circ}C) + 2.3514$.

ACPD
14, 23499–23554, 2014

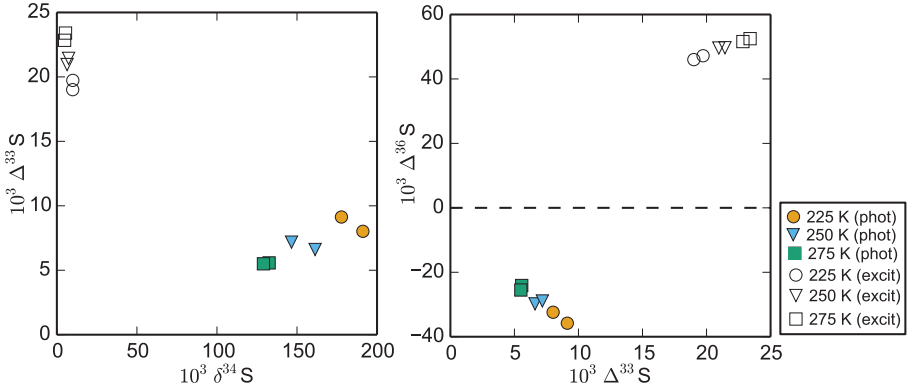

Figure 2. Results of the temperature experiments for SO_2 photolysis and SO_2 photoexcitation (Sect. 2.2). Results from SO_2 photolysis experiments (phot) are shown in filled symbols and SO_2 photoexcitation experiments (excit) are in empty symbols.

ACPD
14, 23499–23554, 2014

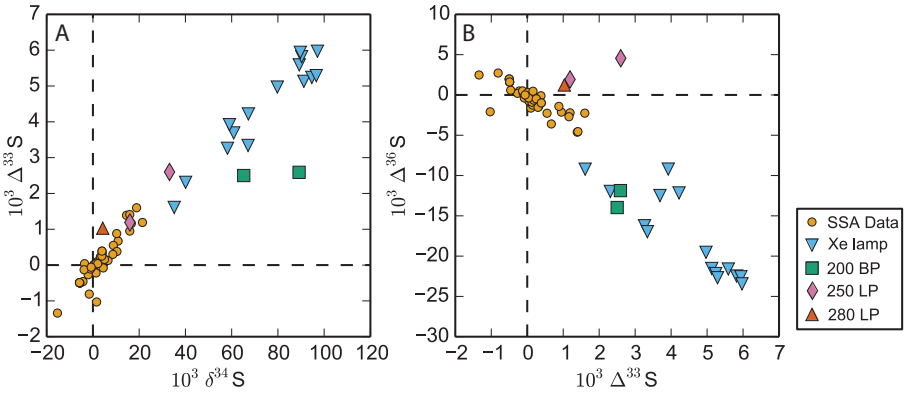

Figure 3. Isotopic results of the $SO_2 + O_2$ experiments described in Sect. 2.3, compared with stratospheric sulfate aerosol samples (SSA Data) from Savarino et al. (2003), Baroni et al. (2007, 2008), Lanciki (2010), and Lanciki et al. (2012).

ACPD
14, 23499–23554, 2014

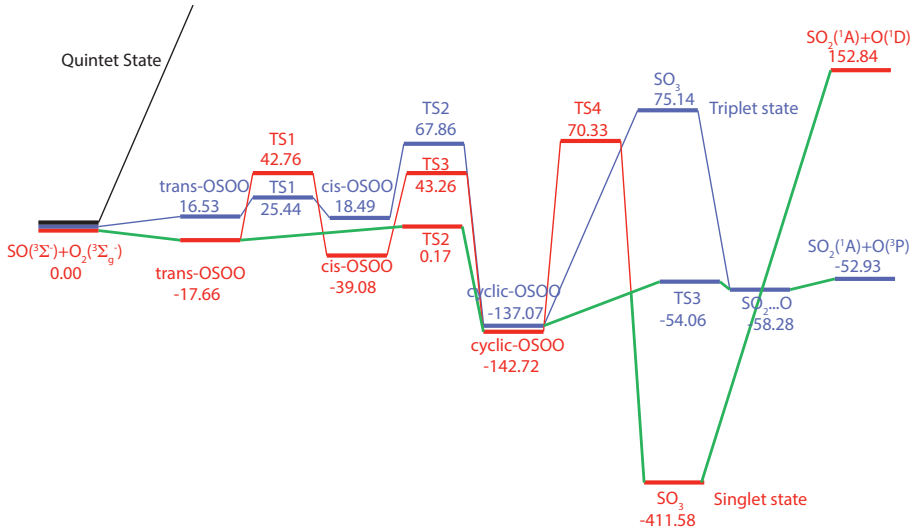

Figure 4. Potential energy profiles on the singlet (red) and triplet (blue) potential energy surfaces for the SO_3 system obtained using B3LYP optimization followed by UCCSD(T)-F12a single point calculation, with the AVTZ basis set. The possible intersystem crossing pathway is depicted by the solid green line. All energies are given in kJ mole^{-1} relative to the $SO(^3\Sigma^-) + O_2(^3\Sigma_g^-)$ asymptote. The quintet (black) state is shown qualitatively due to its high energy.

ACPD
14, 23499–23554, 2014

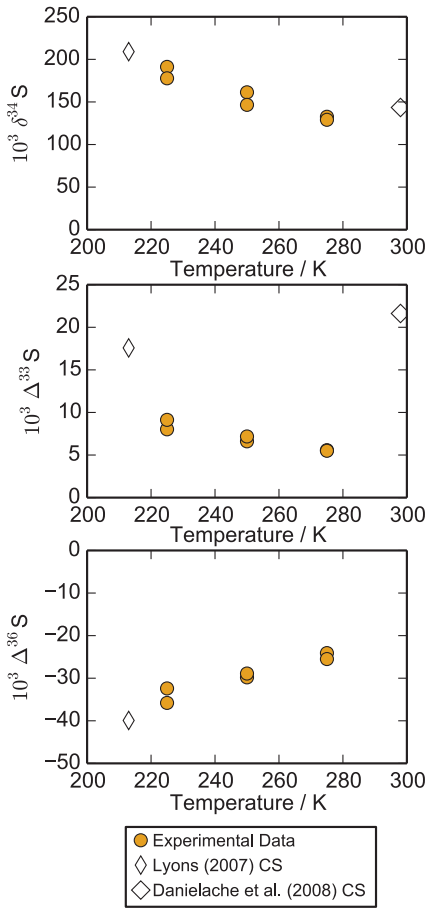

Figure 5. Comparison of SO_2 photolysis temperature experiment results with predictions from isotopologue-specific absorption cross-sections (CS).

ACPD
14, 23499–23554, 2014

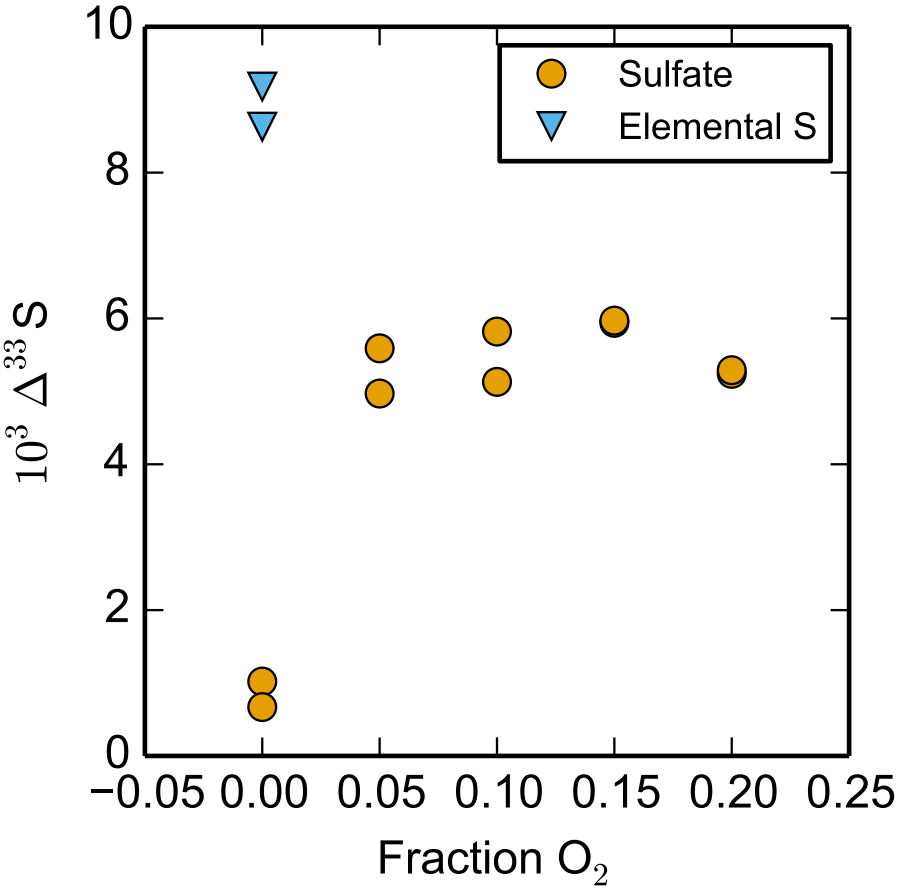

Figure 6. $\Delta^{33}S$ values of sulfate from the photolysis of SO_2 in the presence of O_2 compared with elemental sulfur and sulfate from SO_2 photolysis in the absence of O_2. Conditions are described in Sect. 4.3 and Table 4.

ACPD
14, 23499–23554, 2014

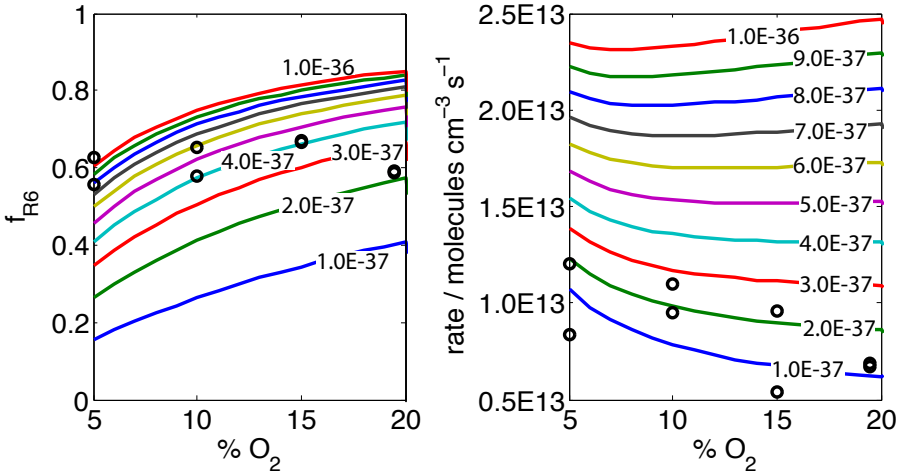

Figure 7. Results of kinetic model (Sect. 4.4, Table 9) compared to experimental data (circles) for f_{R6} (Eq. 5) vs. fraction of SO_3 formed from R6 in the model (left), as well as total SO_3 formation rate (right). Contours on the plot are labeled with the value of rate constant k_{R6} input into the model for a given run.

ACPD
14, 23499–23554, 2014

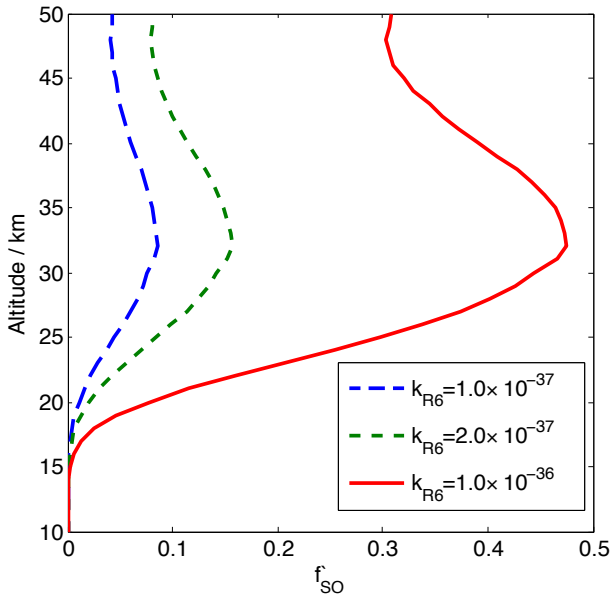

Figure 8. Fraction of sulfate derived from reaction channel R6 (f_{SO}) as a function of altitude for different values of k_{R6}.

ACPD
14, 23499–23554, 2014

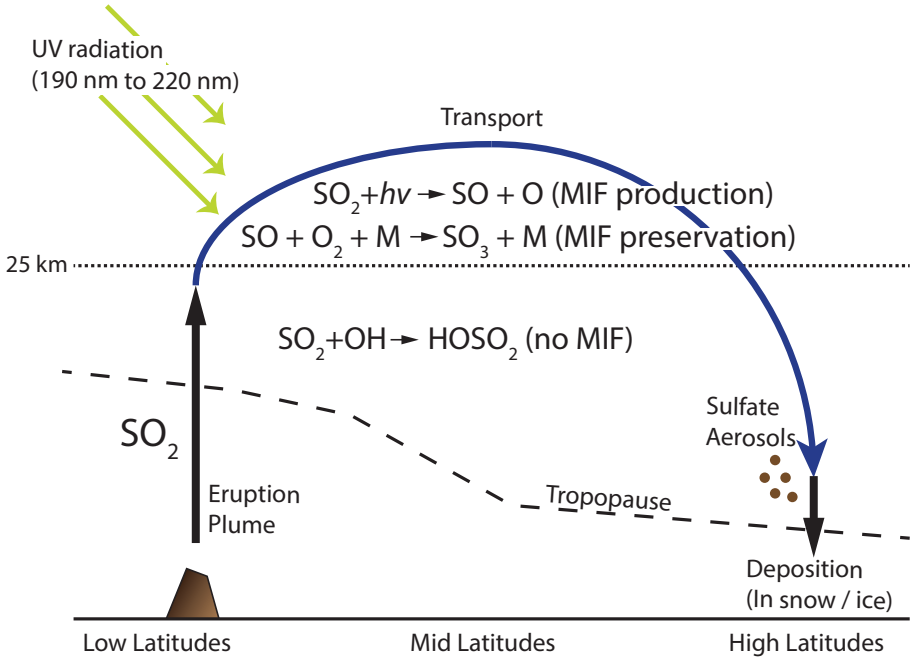

Figure 9. Schematic illustration of the production and preservation of mass-independent fractionation (MIF) in sulfur isotopes following explosive volcanic eruptions. Low latitude eruptions such as Pinatubo (1991) inject large amounts of SO_2 into the stratosphere. Through stratospheric transport, it is brought to altitudes where SO_2 photolysis can occur, producing large MIF signatures. The product of SO_2 photolysis, SO, is preserved via termolecular reaction with O_2. The resulting SO_3 forms sulfate aerosols, which are deposited at high latitudes in polar snow and ice core records. SO_2 oxidation below 25 km is dominantly by OH, which is a mass-dependent process.

ACPD
14, 23499–23554, 2014